

ESTIMATION OF MICROSEISMIC SOURCE
PARAMETERS BY ANISOTROPIC
WAVEFORM INVERSION

by

Oscar Jarillo Michel

© Copyright by Oscar Jarillo Michel, 2015

All Rights Reserved

A thesis submitted to the Faculty and the Board of Trustees of the Colorado School of Mines in partial fulfillment of the requirements for the degree of Master of Science (Geophysics).

Golden, Colorado

Date _____

Signed: _____

Oscar Jarillo Michel

Signed: _____

Dr. Ilya Tsvankin
Thesis Advisor

Golden, Colorado

Date _____

Signed: _____

Dr. Terry Young
Professor and Head
Department of Geophysics

ABSTRACT

In microseismic data processing, source locations and origin times are usually obtained using kinematic techniques, whereas moment-tensor estimates are typically based on linear inversion of P- and S-wave amplitudes. Waveform inversion (WI), which has been used primarily for high-resolution velocity analysis, has the potential to provide more accurate source parameters along with an improved velocity model by incorporating both phase and amplitude information.

The first issue addressed in the thesis is efficient calculation of the gradient of the WI objective function with respect to the model parameters. Application of the adjoint-state method helps obtain closed-form expressions for the gradient with respect to the source location, origin time, and moment tensor. Computation of the forward and adjoint wavefields is performed with a finite-difference algorithm that handles elastic VTI (transversely isotropic with a vertical symmetry axis) models. Numerical examples illustrate the properties of the gradient for multicomponent data recorded by a vertical receiver array placed in homogeneous and horizontally layered VTI media.

Then WI is implemented to estimate the location, origin time, and seismic moment tensor of microseismic sources embedded in 2D VTI media. Both a constant and variable step-length computed by line-search followed by the nonlinear conjugate method (NCG) are used for model updating. Although in the current algorithm the interval VTI parameters are assumed to be known, they can be included in WI at almost no additional cost. Velocity estimation, however, is likely to make the objective function more complicated and increase ambiguity of the inversion. Synthetic tests for data recorded by vertical receiver arrays show that it is possible to tightly constrain all source parameters, if a sufficiently accurate initial model is available. In particular, the source location in layered VTI media can be estimated simultaneously with the moment tensor. The resolution of event location, however,

somewhat decreases when the origin time is unknown or there is an error in one of the VTI parameters.

TABLE OF CONTENTS

ABSTRACT	iii
LIST OF FIGURES	vi
ACKNOWLEDGMENTS	xi
DEDICATION	xiii
CHAPTER 1 INTRODUCTION	1
CHAPTER 2 FORWARD AND INVERSE PROBLEM FOR MICROSEISMIC DATA	5
2.1 Forward problem	5
2.2 Modeling examples	6
2.3 Inverse problem	8
CHAPTER 3 APPLICATION OF THE ADJOINT-STATE METHOD	10
3.1 Implementation	10
3.2 Synthetic tests	12
CHAPTER 4 WAVEFORM INVERSION FOR MICROSEISMIC SOURCE PARAMETERS	20
4.1 Implementation	20
4.2 Properties of the inverse problem	21
4.3 Synthetic tests with a constant step length	22
4.4 Synthetic tests with line search	38
CHAPTER 5 CONCLUSIONS AND RECOMMENDATIONS	46
5.1 Recommendations	48
REFERENCES CITED	50

LIST OF FIGURES

Figure 2.1	2D fault geometry used in forward modeling. The dip angle θ ($0^\circ \leq \theta \leq 90^\circ$) is measured down from the horizontal axis. The incidence plane $[x_1, x_3]$ is assumed to coincide with the dip plane of the fault and contain the slip \mathbf{s}	7
Figure 2.2	Vertical displacement generated by dip-slip sources with different orientation (defined by the angle θ) in a homogeneous VTI medium. The medium parameters are $\rho = 2 \text{ g/cm}^3$, $V_{P0} = 4047 \text{ m/s}$, $V_{S0} = 2638 \text{ m/s}$, $\epsilon = 0.4$, and $\delta = 0$ ($\sigma = 0.94$). The moment tensor is computed from equations 2.9 – 2.11 with $\Sigma \bar{u} = 1 \text{ m}^3$ and (a) $\theta = 0^\circ$, (b) $\theta = 30^\circ$, (c) $\theta = 60^\circ$, and (d) $\theta = 90^\circ$	9
Figure 3.1	Source (white dot) and a vertical line of receivers at $x_1 = 1.2 \text{ km}$ embedded in a homogeneous VTI medium. The receivers are placed at each grid point (every 6 m). The medium parameters are $\rho = 2 \text{ g/cm}^3$, $V_{P0} = 4047 \text{ m/s}$, $V_{S0} = 2638 \text{ m/s}$, $\epsilon = 0.4$, and $\delta = 0$. The source is located at $x_1 = 0.3 \text{ km}$, $x_3 = 0.75 \text{ km}$; $\Sigma \bar{u} = 1 \text{ m}^3$	12
Figure 3.2	Snapshots of the vertical displacement for the model in Figure 3.1 at $t = 0.14 \text{ s}$. (a) The observed wavefield produced by a dip-slip source with $\theta = 0^\circ$. (b) The predicted wavefield from a source with $\theta = 90^\circ$	13
Figure 3.3	Vertical displacement of the (a) observed and (b) predicted data for the model in Figure 3.1.	13
Figure 3.4	Snapshots of the vertical component of the adjoint wavefield for the model in Figure 3.1 at times (a) $t = 0.19 \text{ s}$, (b) $t = 0.26 \text{ s}$, (c) $t = 0.35 \text{ s}$ and (d) $t = 0.44 \text{ s}$. The adjoint wavefield focuses at the actual and trial source locations (which are the same) on plot (d).	14
Figure 3.5	Three-layer VTI model used in the second experiment. The source-receiver geometry is the same as in Figure 3.1. The distance between receivers is 5 m. The parameters $\rho = 2 \text{ kg/m}^3$, $\epsilon = 0.4$, and $\delta = 0$ are the same in all three layers. The vertical velocities in the first layer are $V_{P0} = 4047 \text{ m/s}$ and $V_{S0} = 2638 \text{ m/s}$; for the second layer, $V_{P0} = 4169 \text{ m/s}$ and $V_{S0} = 2320 \text{ m/s}$; for the third layer, $V_{P0} = 4693 \text{ m/s}$ and $V_{S0} = 2682 \text{ m/s}$	16

Figure 3.6	<p>Actual source (white dot), trial source (red dot) and a vertical line of receivers (spacing is 6 m) embedded in a homogeneous VTI medium. The medium parameters are the same as in Figure 3.1. The actual source is located at $x_1 = 0.3$ km, $x_3 = 0.75$ km and the trial source is at $x_1 = 0.32$ km, $x_3 = 0.75$ km. The moment tensor for both sources corresponds to a horizontal ($\theta = 0^\circ$) dip-slip fault with $\Sigma \bar{u} = 1 \text{ m}^3$.</p>	17
Figure 3.7	<p>Two actual sources (white dots), a trial source (red dot), and a vertical line of receivers (the spacing is 6 m) embedded in a homogeneous VTI medium. The medium parameters are the same as in Figure 3.1. The actual sources are located at $x_1 = 0.3$ km, $x_3 = 0.75$ km, and $x_1 = 0.7$ km, $x_3 = 1$ km; the trial source is at $x_1 = 0.42$ km, $x_3 = 0.75$ km. The moment tensor for all three sources corresponds to a horizontal ($\theta = 0^\circ$) dip-slip fault with $\Sigma \bar{u} = 1 \text{ m}^3$.</p>	18
Figure 3.8	<p>Snapshots of the vertical component of the adjoint wavefield for the model in Figure 3.7 at times (a) $t = 0.12$ s, (b) $t = 0.23$ s, (c) $t = 0.33$ s, and (d) $t = 0.44$ s. The adjoint wavefield on plot (d) focuses at both actual source locations and at the trial source location.</p>	19
Figure 4.1	<p>Dependence of the objective function $\mathcal{F}(\mathbf{m})$ on the trial source parameters (a) x_1^s, (b) x_3^s, and (c) t_0 for a homogeneous VTI model. The global minimum coincides with the actual parameter value. The components of the tensor \mathbf{M} are fixed at the actual values. The medium parameters are $\rho = 2 \text{ g/cm}^3$, $V_{P0} = 4047 \text{ m/s}$, $V_{S0} = 2638 \text{ m/s}$, $\epsilon = 0.4$, and $\delta = 0$.</p>	23
Figure 4.2	<p>Actual source (white dot), trial source (red dot) and a vertical line of receivers (spacing is 6 m) embedded in a homogeneous VTI medium. The medium parameters are $\rho = 2 \text{ g/cm}^3$, $V_{P0} = 4047 \text{ m/s}$, $V_{S0} = 2638 \text{ m/s}$, $\epsilon = 0.4$, and $\delta = 0$. The actual source is located at $x_1 = 0.3$ km and $x_3 = 0.75$ km with $\theta = 0^\circ$ (see equations 2.9 – 2.11). For the trial source, $x_1 = 0.32$ km, $x_3 = 0.8$ km, and $\theta = 15^\circ$. Both events occur at the same time ($t_0 = 0.049$ s) and have the same $\Sigma \bar{u} = 1 \text{ m}^3$.</p>	24
Figure 4.3	<p>Change of the normalized objective function $\mathcal{F}(\mathbf{m})$ with iterations for the model in Figure 4.2.</p>	24
Figure 4.4	<p>Change of the source coordinates (a) x_1^s and (b) x_3^s with iterations for the model in Figure 4.2. The actual values are marked by dashed lines.</p>	25
Figure 4.5	<p>Change of the moment-tensor elements (a) M_{11}, (b) M_{33}, and (c) M_{13} with iterations for the model in Figure 4.2. The actual values are marked by dashed lines.</p>	26

Figure 4.6	Source (white dot) and a vertical line of receivers (spacing is 6 m) embedded in a homogeneous VTI medium. The medium parameters are the same as in Figure 4.2. The location of the actual and trial sources is the same: $x_1 = 0.3$ km and $x_3 = 0.75$ km, as well as $\Sigma \bar{u} = 1$ m ³ . For the actual source, $t_0 = 0.049$ s and $\theta = 0^\circ$, for the trial source, $t_0 = 0.042$ s and $\theta = 15^\circ$	27
Figure 4.7	Change of the normalized objective function $\mathcal{F}(\mathbf{m})$ with iterations for the model in Figure 4.6.	27
Figure 4.8	Change of the origin time t_0 with iterations for the model in Figure 4.6.	28
Figure 4.9	Change of the moment-tensor elements (a) M_{11} , (b) M_{33} , and (c) M_{13} with iterations for the model in Figure 4.6.	29
Figure 4.10	Actual (white dot) and trial (red dot) sources and a vertical receiver array in a five-layer VTI model. The receiver geometry is the same as in Figure 4.2. The parameters $\rho = 2$ kg/m ³ , $\epsilon = 0.4$, and $\delta = 0$ are the same in all five layers. The vertical velocities in the top layer are $V_{P0} = 4419$ m/s and $V_{S0} = 2645$ m/s; for the second layer, $V_{P0} = 4956$ m/s and $V_{S0} = 2424$ m/s; for the third layer, $V_{P0} = 4048$ m/s and $V_{S0} = 2638$ m/s; for the fourth layer, $V_{P0} = 4170$ m/s and $V_{S0} = 2320$ m/s; for the fifth layer, $V_{P0} = 4694$ m/s and $V_{S0} = 2682$ m/s. The actual source is located at $x_1 = 0.3$ km and $x_3 = 0.75$ km with $\theta = 0^\circ$. The trial source is located at $x_1 = 0.32$ km and $x_3 = 0.8$ km with , and $\theta = 15^\circ$. Both events occur at the same time ($t_0 = 0.035$ s) and have the same $\Sigma \bar{u} = 1$ m ³	30
Figure 4.11	Change of the normalized objective function $\mathcal{F}(\mathbf{m})$ with iterations for the model in Figure 4.10. All source parameters are unknown.	31
Figure 4.12	Change of the source coordinates (a) x_1^s and (b) x_3^s with iterations for the model in Figure 4.10.	31
Figure 4.13	Change of the origin time t_0 with iterations for the model in Figure 4.10.	32
Figure 4.14	Change of the normalized objective function $\mathcal{F}(\mathbf{m})$ with iterations for the model in Figure 4.10. The origin time t_0 is fixed at the correct value.	32
Figure 4.15	Change of the source coordinates (a) x_1^s and (b) x_3^s with iterations for the model in Figure 4.10. The origin time t_0 is fixed at the correct value.	33
Figure 4.16	Change of the moment-tensor elements (a) M_{11} , (b) M_{33} , and (c) M_{13} with iterations for the model in Figure 4.10. The origin time t_0 is fixed at the correct value.	34

Figure 4.17	Change of the normalized objective function $\mathcal{F}(\mathbf{m})$ with iterations for the model in Figure 4.2. The inversion is performed with an incorrect value of ϵ ($\epsilon = 0.3$ instead of the actual 0.4). The rest of the VTI parameters are unchanged.	35
Figure 4.18	Change of the source coordinates (a) x_1^s and (b) x_3^s with iterations for the model in Figure 4.2. The inversion uses $\epsilon = 0.3$ instead of the actual $\epsilon = 0.4$	35
Figure 4.19	Change of the moment-tensor elements (a) M_{11} , (b) M_{33} , and (c) M_{13} with iterations for the model in Figure 4.2. The inversion uses $\epsilon = 0.3$ instead of the actual $\epsilon = 0.4$	36
Figure 4.20	Vertical displacement of the observed data contaminated with Gaussian noise for the model in Figure 4.2. The noise has the same frequency band as the data and the variance is equal to 0.07% of the maximum amplitude.	37
Figure 4.21	Change of the normalized objective function $\mathcal{F}(\mathbf{m})$ with iterations for the model in Figure 4.2. The inversion was performed on noise-contaminated data (see Figure 4.20).	37
Figure 4.22	Change of the source coordinates (a) x_1^s and (b) x_3^s with iterations for the model in Figure 4.2. The inversion was performed on noise-contaminated data (see Figure 4.20).	38
Figure 4.23	Change of the moment-tensor elements (a) M_{11} , (b) M_{33} , and (c) M_{13} with iterations for the model in Figure 4.2. The inversion was performed on noise-contaminated data (see Figure 4.20).	39
Figure 4.24	Change of the normalized objective function $\mathcal{F}(\mathbf{m})$ with iterations for the model in Figure 4.2. Parameter updating was carried out with the NCG method. The origin time t_0 is fixed at the correct value.	41
Figure 4.25	Change of the source coordinates (a) x_1^s and (b) x_3^s with iterations for the model in Figure 4.2. Parameter updating was carried out with the NCG method.	41
Figure 4.26	Change of the moment-tensor elements (a) M_{11} , (b) M_{33} , and (c) M_{13} with iterations for the model in Figure 4.2. Parameter updating was carried out with the NCG method.	42

Figure 4.27	Change of the normalized objective function $\mathcal{F}(\mathbf{m})$ with iterations for the model in Figure 4.2. Parameter updating was carried out with the NCG method followed by optimization with a constant step length. The origin time t_0 is fixed at the correct value.	44
Figure 4.28	Change of the source coordinates (a) x_1^s and (b) x_3^s with iterations for the model in Figure 4.10. Parameter updating was carried out with the NCG method followed by optimization with a constant step length. . . .	44
Figure 4.29	Change of the moment-tensor elements (a) M_{11} , (b) M_{33} , and (c) M_{13} with iterations for the model in Figure 4.2. Parameter updating was carried out with the NCG method followed by optimization with a constant step length.	45

ACKNOWLEDGMENTS

The project presented in this thesis started as a suggestion by Vladimir Grechka during the 2012 CWP Project Review Meeting. At that point I did not know much about micro-seismicity and FWI, but eventually I was able to become familiar with these topics and to continue developing the ideas initially presented by Vladimir.

First, I am deeply grateful to my advisor, Ilya Tsvankin for all the support, guidance, confidence and especially for the patience he has shown with me throughout my M.S. study. The knowledge I acquired during his seismology classes helped me make significant progress in my research and better understand topics such as anisotropy. Also special thanks to CWP for providing the necessary financial support for my studies over the last few years.

The classes I took with Paul Sava were very important and helped introduce me to the world of seismic inversion and imaging. Tom Davis, Luis Tenorio, and Manika Prasad kindly accepted being part of my committee and provided valuable feedback on this thesis.

Thanks also to Vladimir Grechka for suggesting this project when I was looking for one. He has also been an important source of valuable insights regarding different aspects of this work. Whenever I have asked a question regarding the project, he has kindly answered it. I would also like to thank Jeroen Tromp for his comments regarding the calculation of the gradient, and Gerhard Pratt for his help with FWI and step-length calculation.

Many thanks to Pam and Shingo for all the work they do in CWP, and Diane for all the support related to writing and academic life in general. I also would like to thank John Stockwell for his help in providing many of the computational tools employed here. Without his help, this work would not have succeeded.

I would also like to acknowledge the help of many students in CSM and CWP, particularly Esteban Díaz Pantin, Nishant Kamath, Francesco Perrone, and Steve Smith for their helpful advice and assistance regarding the technical aspects, especially during the first stages of

the project.

Being a CWP student would not be possible without the knowledge I acquired in Mexico before coming here. Thanks to many people, in particular Gerardo Ronquillo Jarillo, for his teachings and help in supporting my decision to study abroad.

Finally, I thank my family, especially my parents and brother. Their unconditional support, advice, and love has always helped me move forward.

To my parents, Olivia and Oscar.

CHAPTER 1

INTRODUCTION

Microseismicity has developed in recent years as an efficient technique for monitoring of hydraulic fractures and the surrounding reservoir volume (Kendall et al., 2011; Maxwell, 2010). Microseismic experiments typically involve recording the seismic response to hydraulic fracturing of tight reservoirs, most often shales. The location of the induced microfractures, as well as the origin time of the corresponding seismic events, can be inferred from the data acquired in an observation borehole or at the surface. Usually only a single borehole is available, but it is highly beneficial to record microseismic data in several boreholes.

Accurate location of microseismic events requires knowledge of the background velocity model. The initial model is usually obtained from sonic logs and traveltimes of the direct P- and S-waves excited by perforation shots and recorded by geophones deployed in a monitor borehole. Afterwards, the model can be updated using the traveltimes or waveforms of microseismic events. Velocity analysis without adequately accounting for seismic anisotropy may lead to significant errors in event location (Van Dok et al., 2011). In particular, shales are known to be transversely isotropic and may become orthorhombic or possess an even lower symmetry due to fracturing (Tsvankin, 2012; Tsvankin and Grechka, 2011).

Depending on the receiver geometry and spatial distribution of sources, microseismic data can help estimate the pertinent anisotropy parameters (Grechka and Duchkov, 2011) simultaneously with event location. For example, Grechka et al. (2011) demonstrate that anisotropic velocity models constructed from traveltimes while locating microseismic events provide more accurate source locations than those obtained without accounting for anisotropy. Also, Li et al. (2013) show that building VTI velocity models simultaneously with event location significantly reduces the traveltime residuals compared to standard location techniques that employ isotropic velocity models obtained from sonic logs and perforation shots. Grechka

and Yaskevich (2013, 2014) demonstrate that for microseismic surveys with sufficient angle coverage it is possible to construct even layered triclinic (i.e., most general anisotropic) models and substantially improve the accuracy of event location.

Still, kinematic inversion essentially replaces a seismic trace with the δ -functions corresponding to the traveltimes of the direct arrivals, which restricts the resolution of event location according to the Rayleigh criterion (i.e., two sources are indistinguishable if the distance between them is smaller than one-half of the predominant wavelength). Considering the rapidly increasing usage of back-projection techniques and the rich information content of microseismic data, improved results can be expected from waveform inversion (WI). Indeed, WI operates with the entire trace including scattered waves, so location results are not subject to the Rayleigh criterion. Hence, for wavelengths typical in downhole microseismic surveys, one can expect substantially reduced event-location errors. Another potential benefit of WI, not explored in this thesis, is an improved accuracy of the velocity model.

Whereas the main goal of microseismic surveys is to estimate the source locations \mathbf{x}^s , it is also essential to obtain the event origin time t_0 and evaluate the source mechanism, which can reveal important information about the rupture process. Point earthquake sources are described by the second-rank symmetric seismic moment tensor \mathbf{M} . As discussed by Vavryčuk (2007), all six independent elements of \mathbf{M} for microseismic events can be retrieved from the amplitudes of P-waves recorded in three boreholes or from P-, SV-, and SH-wave amplitudes measured in two boreholes. For sources and receivers located in the $[x_1, x_3]$ -plane of a VTI model, the in-plane polarized waves depend on the moment-tensor elements M_{11} , M_{13} , and M_{33} , which potentially can be found by inverting P- and SV-waveforms recorded in a single borehole.

Most existing techniques invert for source location, origin time, and moment tensor \mathbf{M} separately. For instance, in practice \mathbf{M} is often estimated by linear inversion of P- and S-wave amplitudes under the assumption that \mathbf{x}^s and t_0 are known. In contrast, since WI incorporates information about the entire trace, it has the potential of resolving all these

parameters simultaneously and with high accuracy from multicomponent seismic data.

Waveform inversion is a nonlinear optimization technique based on full-wavefield modeling, which is designed to include phase and, sometimes, amplitude information (Gauthier et al., 1986; Mora, 1987; Pratt, 1999) in building subsurface models. As first suggested by Lailly (1983) and Tarantola (1984), back-propagation in time of the data residuals followed by cross-correlation of the resulting wavefield with the forward-propagated wavefield helps iteratively construct high-resolution velocity models. An overview of the progress in the development of WI methods can be found in Virieux and Operto (2009). Applications of WI in exploration seismology have been mostly limited to velocity tomography. Seismic waveforms, however, contain information that can be used to constrain other important quantities, such as parameters of earthquake sources, which are essential in microseismic monitoring. Recently, WI has been extended to elastic (Lee et al., 2010) and anisotropic media (Kamath and Tsvankin, 2013), which makes it appropriate for multicomponent reflection or microseismic data.

The objective function in WI quantifies the difference between the observed and predicted data in the time or frequency domain. Efficient inversion requires application of iterative optimization schemes such as gradient-based methods, which involve calculation of the gradient of the objective function with respect to the model parameters. In principle, the gradient can be found from the Fréchet derivatives obtained by differentiating the wavefield with respect to each model parameter. However, if the number of unknowns is large, computation of the Fréchet derivatives becomes prohibitively expensive.

A computationally efficient alternative for computing the gradient without the Fréchet derivatives is the adjoint-state method (Fichtner, 2006, 2009; Köhn, 2011; Lions, 1972; Plessix, 2006). The main advantage of this method (Talagrand and Courtier, 1987) is that the gradient for all model parameters is computed using only two numerical-modeling simulations: one to generate the forward wavefield (predicted data), and the other to compute the adjoint wavefield.

There has been significant progress in applying adjoint methods to tomographic velocity analysis and source-parameter inversion in global seismology. Tromp et al. (2005) and Liu and Tromp (2006) employ an adjoint formulation based on the Lagrangian-multiplier method to derive the gradient for estimating the P- and S-wave velocities in isotropic media from waveform inversion. They also analyze the sensitivity (Fréchet) kernels for 2D and 3D velocity models. Kim et al. (2011) obtain gradient expressions for the source parameters using the adjoint-state method. They also implement nonlinear conjugate-gradient inversion to estimate the source location and moment tensor for two earthquakes in Southern California using a known isotropic velocity model. Morency and Mellors (2012) follow the same approach to evaluate the source parameters of a geothermal event.

In Chapter 2, I start by describing 2D elastic finite-difference modeling for dislocation-type sources embedded in a VTI medium. To illustrate the modeling procedure and wavefield properties, examples using different fault orientations are included. The modeling results are used to provide a description of the main quantities involved in the microseismic inverse problem.

Chapter 3 employs the adjoint-state method to compute the gradient for waveform inversion of microseismic data. Efficient gradient calculation is implemented by adapting to our problem the general expressions for the WI gradient obtained by Kim et al. (2011). The performance of the algorithm is illustrated by synthetic tests for homogeneous and layered VTI media.

Chapter 4 presents a 2D methodology for estimating the parameters \mathbf{x}^s , t_0 , and \mathbf{M} using waveform inversion. This methodology employs an iterative local gradient-descent algorithm for simultaneous updating of all source parameters. The inversion involves the so-called nondimensionalization approach (Kim et al., 2011) because the model parameters belong to different classes (i.e., have different units). A constant step length and a step length calculated by a line search algorithm followed by the NCG method are used for model updating. Although the interval Thomsen parameters of layered VTI media potentially can be esti-

mated by WI as well, velocity analysis is beyond the scope of the current implementation. The methodology is tested on multicomponent synthetic data generated for microseismic experiments in homogeneous and horizontally layered VTI media.

CHAPTER 2

FORWARD AND INVERSE PROBLEM FOR MICROSEISMIC DATA

Estimating the source parameters from microseismic data using WI requires modeling capable of simulating radiation from dislocation-type sources. Here, I describe simulation of wavefields from dislocation-type sources using a finite-difference scheme that handles elastic wave propagation in VTI media. Numerical results illustrate the wavefield properties in a homogeneous VTI medium for different fault-plane orientations. After describing the modeling algorithm, I discuss the formulation of the inverse problem designed to estimate the source parameters.

2.1 Forward problem

The wave equation for a heterogeneous anisotropic medium can be written as:

$$\rho \frac{\partial^2 u_i}{\partial t^2} - \frac{\partial}{\partial x_j} \left(c_{ijkl} \frac{\partial u_k}{\partial x_l} \right) = f_i, \quad (2.1)$$

where $\mathbf{u}(\mathbf{x}, t)$ is the displacement field, t is time, c_{ijkl} is the stiffness tensor ($i, j, k, l = 1, 2, 3$), $\rho(\mathbf{x})$ is density, and $\mathbf{f}(\mathbf{x}, t)$ is the body force. Summation over repeated indices is implied.

Dislocation-type sources are described by the seismic moment tensor (e.g., Jost and Herrmann, 1989),

$$\mathbf{M} = \begin{pmatrix} M_{11} & M_{12} & M_{13} \\ M_{21} & M_{22} & M_{23} \\ M_{31} & M_{32} & M_{33} \end{pmatrix}, \quad (2.2)$$

which can be incorporated into the source term of equation 2.1 by using the notion of equivalent force (Aki and Richards, 1980; Dahlen and Tromp, 1998):

$$\rho \frac{\partial^2 u_i}{\partial t^2} - \frac{\partial}{\partial x_j} \left(c_{ijkl} \frac{\partial u_k}{\partial x_l} \right) = -M_{ij} \frac{\partial[\delta(\mathbf{x} - \mathbf{x}^s)]}{\partial x_j} S(t), \quad (2.3)$$

where \mathbf{x}^s is the source location, $S(t)$ is the source time function, and $\delta(\mathbf{x} - \mathbf{x}^s)$ is the spatial δ -function. I use a finite-difference (FD) algorithm to obtain exact solutions of equation 2.3.

2.2 Modeling examples

Forward modeling for gradient calculation in VTI media is carried out with the elastic finite-difference program `sfewe` in `MADAGASCAR`. The model is described by the interval Thomsen parameters — the P- and S-wave vertical velocities V_{P0} and V_{S0} and the anisotropy coefficients ϵ and δ defined as (Thomsen, 1986; Tsvankin, 2012):

$$\epsilon \equiv \frac{c_{11} - c_{33}}{2c_{33}}, \quad (2.4)$$

$$\delta \equiv \frac{(c_{13} + c_{55})^2 - (c_{33} - c_{55})^2}{2c_{33}(c_{33} - c_{55})}. \quad (2.5)$$

Note that P- and SV-waves propagating in the $[x_1, x_3]$ -plane are not influenced by the Thomsen parameter γ . The coefficient $\sigma \equiv (V_{P0}/V_{S0})^2(\epsilon - \delta)$ is an important parameter combination which is largely responsible for the kinematic signatures of SV-waves.

The relevant elements of the moment tensor \mathbf{M} of a dislocation-type source for the in-plane polarized waves (P and SV) in a VTI medium can be represented as (Aki and Richards, 1980; Vavryčuk, 2005):

$$M_{11} = \Sigma \bar{u} \nu_3 s_3 (c_{13} - c_{11}), \quad (2.6)$$

$$M_{13} = \Sigma \bar{u} (\nu_1 s_3 + \nu_3 s_1) c_{55}, \quad (2.7)$$

$$M_{33} = \Sigma \bar{u} \nu_3 s_3 (c_{33} - c_{13}), \quad (2.8)$$

where Σ is the fault area, \bar{u} is the magnitude of slip (displacement discontinuity), $\boldsymbol{\nu}$ is the unit fault normal, \mathbf{s} is the unit vector in the slip direction, and c_{11} , c_{13} , c_{33} , and c_{55} are the stiffness coefficients in the two-index Voigt notation (Figure 2.1). Because the vectors $\boldsymbol{\nu}$ and \mathbf{s} are confined to the $[x_1, x_3]$ -plane, equations 2.6 – 2.8 for dip-slip sources can be expressed as a function of the fault dip angle θ . Taking into account that $\nu_1 = \sin \theta$, $\nu_3 = \cos \theta$, $s_1 = \cos \theta$, and $s_3 = -\sin \theta$, equations 2.6 – 2.8 can be rewritten as:

$$M_{11} = -\frac{\Sigma \bar{u}}{2} \sin 2\theta (c_{13} - c_{11}), \quad (2.9)$$

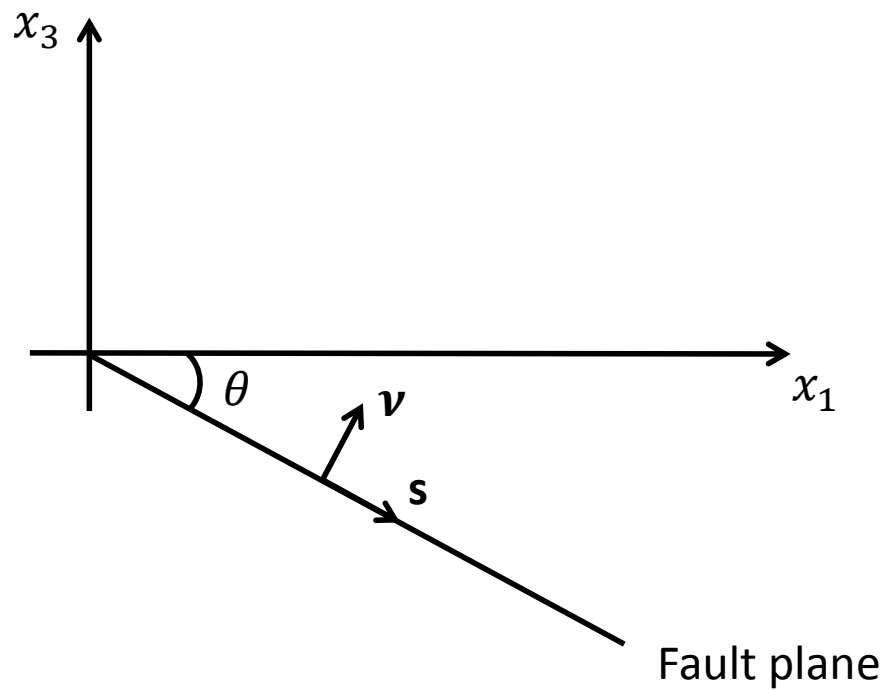


Figure 2.1: 2D fault geometry used in forward modeling. The dip angle θ ($0^\circ \leq \theta \leq 90^\circ$) is measured down from the horizontal axis. The incidence plane $[x_1, x_3]$ is assumed to coincide with the dip plane of the fault and contain the slip s .

$$M_{13} = \Sigma \bar{u} \cos 2\theta c_{55} , \quad (2.10)$$

$$M_{33} = -\frac{\Sigma \bar{u}}{2} \sin 2\theta (c_{33} - c_{13}) . \quad (2.11)$$

The wavefields generated by dislocation-type sources in a homogeneous VTI medium are shown in Figure 2.2. The amplitude distribution and intensity of the P- and S-waves change substantially with the fault orientation. Because σ is positive and relatively large (close to unity), the SV-wavefront exhibits triplications at oblique propagation directions (Tsvankin, 2012). The P-wavefront is substantially extended in the horizontal direction because $\epsilon = 0.4$.

2.3 Inverse problem

As mentioned above, the P- and SV-waves recorded in the $[x_1, x_3]$ -plane depend on the components M_{11} , M_{13} , and M_{33} of the moment tensor. Here, our goal is to invert just for the three moment-tensor elements, the source coordinates x_1^s and x_3^s , and the origin time t_0 assuming that the velocity model is known. Hence, the vector of unknown model parameters is defined as:

$$\mathbf{m} = \{x_1^s, x_3^s, t_0, M_{11}, M_{13}, M_{33}\} . \quad (2.12)$$

In synthetic tests, the observed displacement \mathbf{d}_{obs} and predicted displacement $\mathbf{d}_{\text{pre}}(\mathbf{m})$ are produced by two forward simulations, with \mathbf{d}_{pre} computed after perturbing the source parameters used to generate \mathbf{d}_{obs} . The elastic displacement field $\mathbf{u}(\mathbf{x}^s, \mathbf{x}^{r_n}, t)$ in both simulations is excited by a single source at \mathbf{x}^s and recorded by N receivers located at \mathbf{x}^{r_n} ($n = 1, 2, \dots, N$). The data residuals are measured by the least-squares objective function \mathcal{F} , which is minimized by the inversion algorithm:

$$\mathcal{F}(\mathbf{m}) = \frac{1}{2} \|\mathbf{d}_{\text{pre}}(\mathbf{m}) - \mathbf{d}_{\text{obs}}\|^2 . \quad (2.13)$$

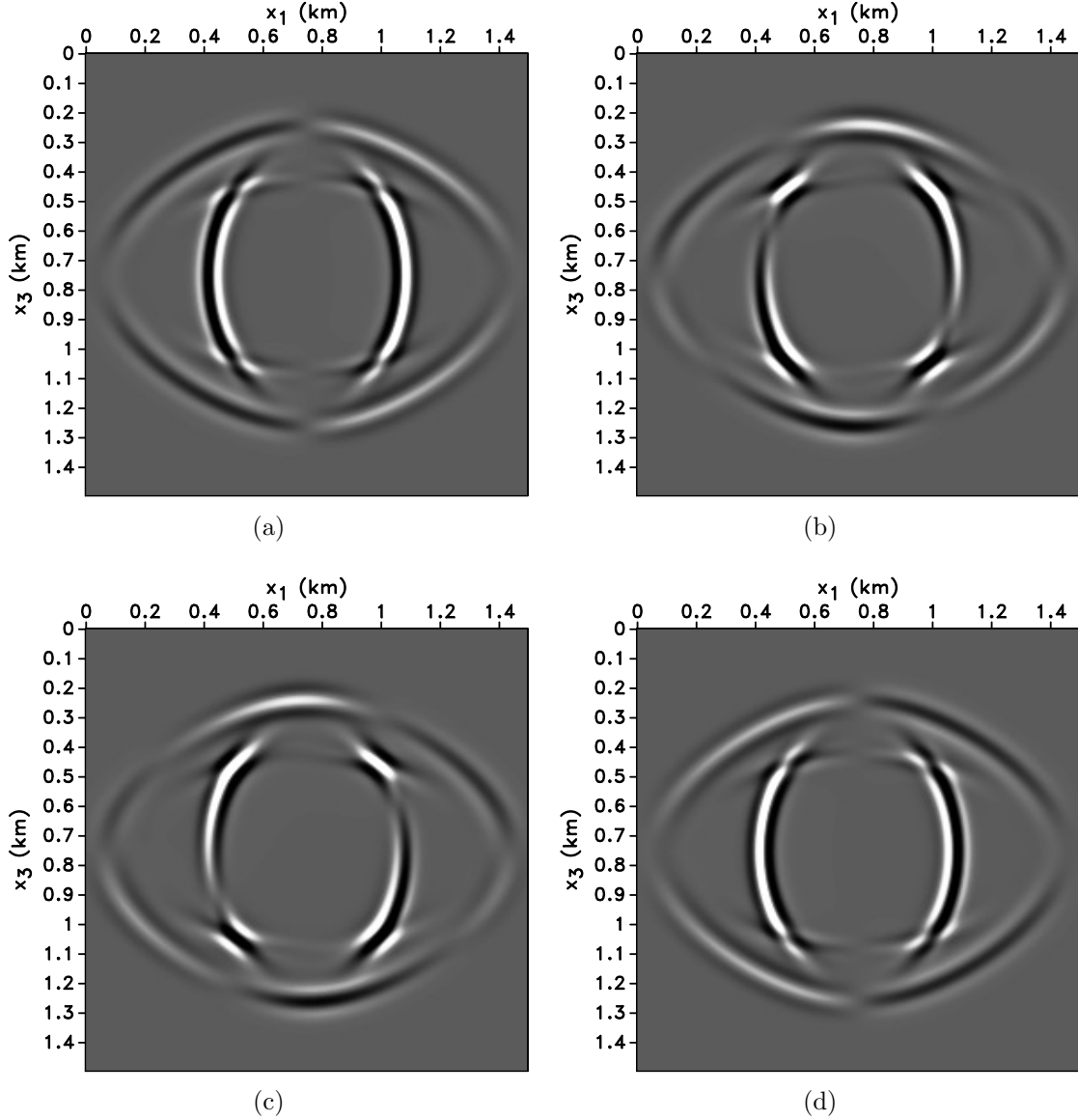


Figure 2.2: Vertical displacement generated by dip-slip sources with different orientation (defined by the angle θ) in a homogeneous VTI medium. The medium parameters are $\rho = 2$ g/cm³, $V_{P0} = 4047$ m/s, $V_{S0} = 2638$ m/s, $\epsilon = 0.4$, and $\delta = 0$ ($\sigma = 0.94$). The moment tensor is computed from equations 2.9 – 2.11 with $\Sigma \bar{u} = 1$ m³ and (a) $\theta = 0^\circ$, (b) $\theta = 30^\circ$, (c) $\theta = 60^\circ$, and (d) $\theta = 90^\circ$.

CHAPTER 3

APPLICATION OF THE ADJOINT-STATE METHOD

One of the main issues in implementing WI is calculation of the gradient of the objective function. In general, this is a computationally expensive process since it involves the sensitivity of the forward wavefield with respect to perturbations in the model parameters. In this section, the adjoint-state method is employed to calculate the gradient for microseismic source parameters.

3.1 Implementation

The objective function depends on the model parameters through the state variables, which represent the solution of the forward-modeling equations. In this case, the state variable is the elastic displacement field $\mathbf{u}(\mathbf{x}, t)$ generated by a microseismic source and governed by equation 2.3.

Iterative optimization techniques involve calculation of the model update at each iteration. The update direction is determined by the gradient (the derivatives of the objective function with respect to the model parameters), $\partial\mathcal{F}(\mathbf{m})/\partial\mathbf{m}$. The adjoint-state method is designed to find the gradient for the entire set of model parameters in just two modeling simulations. However, because this method does not calculate the Fréchet derivatives, it is impossible to evaluate the sensitivity of the solution to perturbation errors.

The adjoint-state method involves the following main steps e.g.,(Perrone and Sava, 2012):

1. Computation of the state variable (forward wavefield).
2. Computation of the adjoint source.
3. Computation of the adjoint-state variable (adjoint wavefield).
4. Computation of the gradient.

In addition to equation 2.3, the method requires solving the adjoint wave equation:

$$\rho \frac{\partial^2 u_i^\dagger}{\partial t^2} - c_{ijkl} \frac{\partial^2 u_k^\dagger}{\partial x_j \partial x_l} = \sum_{n=1}^N (\mathbf{d}_{\text{obs}} - \mathbf{d}_{\text{pre}})(T - t) \delta(\mathbf{x} - \mathbf{x}^{\Gamma_n}), \quad (3.1)$$

where \mathbf{u}^\dagger is called the ‘‘adjoint wavefield.’’ The so-called adjoint source on the right-hand side of equation 3.1 is obtained by differentiating the objective function $\mathcal{F}(\mathbf{m})$ with respect to the forward wavefield \mathbf{u} , and consists of the time-reversed data residuals. Therefore, the adjoint simulation can be carried out with the same modeling code by ‘‘injecting’’ the adjoint source at the receiver locations and then running the forward simulation.

The derivatives of the objective function with respect to the moment-tensor elements, source coordinates, and origin time can be found as (Kim et al., 2011):

$$\frac{\partial \mathcal{F}}{\partial M_{ij}} = \int_0^T \epsilon_{ij}^\dagger(\mathbf{x}^{\text{ts}}, t) S(T - t) dt, \quad (3.2)$$

$$\frac{\partial \mathcal{F}}{\partial x_i^s} = \int_0^T \frac{\partial [\mathbf{M} : \boldsymbol{\epsilon}^\dagger(\mathbf{x}^{\text{ts}}, t)]}{\partial x_i} \Big|_{\mathbf{x}^{\text{ts}}} S(T - t) dt, \quad (3.3)$$

$$\frac{\partial \mathcal{F}}{\partial t_0} = \int_0^T \mathbf{M} : \boldsymbol{\epsilon}^\dagger(\mathbf{x}^{\text{ts}}, t) \frac{\partial S(T - t)}{\partial t} dt, \quad (3.4)$$

where \mathbf{x}^{ts} is the trial source location, T is the recording time, $\boldsymbol{\epsilon}^\dagger = \frac{1}{2}[\nabla \mathbf{u}^\dagger + (\nabla \mathbf{u}^\dagger)^T]$ is defined as the adjoint strain tensor, and $\mathbf{M} : \boldsymbol{\epsilon}^\dagger$ is the double inner product of the tensors \mathbf{M} and $\boldsymbol{\epsilon}^\dagger$. Equations 3.2 – 3.4 applied to the 2D problem yield the gradient vector \mathbf{g} for the six source parameters:

$$\mathbf{g} = \left\{ \frac{\partial \mathcal{F}}{\partial M_{11}}, \frac{\partial \mathcal{F}}{\partial M_{13}}, \frac{\partial \mathcal{F}}{\partial M_{33}}, \frac{\partial \mathcal{F}}{\partial x_1^s}, \frac{\partial \mathcal{F}}{\partial x_3^s}, \frac{\partial \mathcal{F}}{\partial t_0} \right\}. \quad (3.5)$$

It is interesting that in contrast to the gradient for velocity-related parameters (Liu and Tromp, 2006), which depends on the interaction between the forward and adjoint wavefields, equations 3.2 – 3.4 include only the adjoint wavefield. This means that there is no need to store or recalculate the forward wavefield during gradient calculation.

When the adjoint-state method is applied to velocity analysis, the adjoint wavefield \mathbf{u}^\dagger is supposed to ‘‘illuminate’’ the erroneous parts of the velocity model. Likewise, for the source-

inversion problem, \mathbf{u}^\dagger reveals the difference in \mathbf{M} , \mathbf{x}^s , and t_0 that produces the mismatch between the observed and predicted data.

In principle, the number of sources in the adjoint problem is unrestricted. If the forward wavefield is excited by multiple sources, the adjoint wavefield may focus at the actual as well as perturbed (trial) source locations. These areas of focusing make the main contribution to the gradient. However, for inversion purposes the derivatives in equations 3.2 – 3.4 are needed only at the trial source position.

Note that the derivatives for \mathbf{x}^s and t_0 (equations 3.3 and 3.4) include the double-inner product $\mathbf{M} : \boldsymbol{\epsilon}^\dagger(\mathbf{x}^{ts}, t)$, which involves summation over all elements of \mathbf{M} . Due to this dependence, stable inversion for \mathbf{x}^s and t_0 requires an accurate initial model for the moment tensor.

3.2 Synthetic tests

Next, I present the results of synthetic tests for gradient calculation in homogeneous and layered VTI media, with the wavefield modeled using the FD code mentioned above.

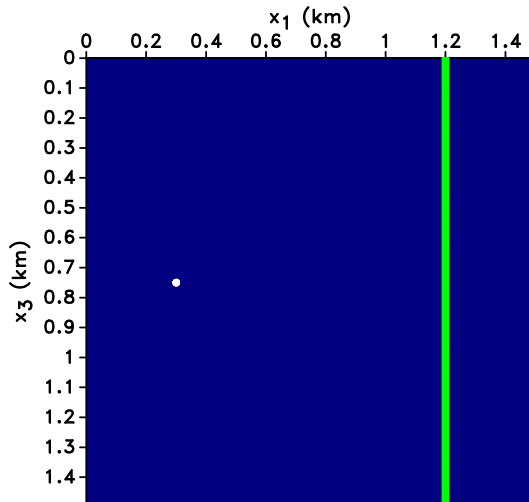


Figure 3.1: Source (white dot) and a vertical line of receivers at $x_1 = 1.2$ km embedded in a homogeneous VTI medium. The receivers are placed at each grid point (every 6 m). The medium parameters are $\rho = 2$ g/cm³, $V_{P0} = 4047$ m/s, $V_{S0} = 2638$ m/s, $\epsilon = 0.4$, and $\delta = 0$. The source is located at $x_1 = 0.3$ km, $x_3 = 0.75$ km; $\Sigma \bar{u} = 1$ m³.

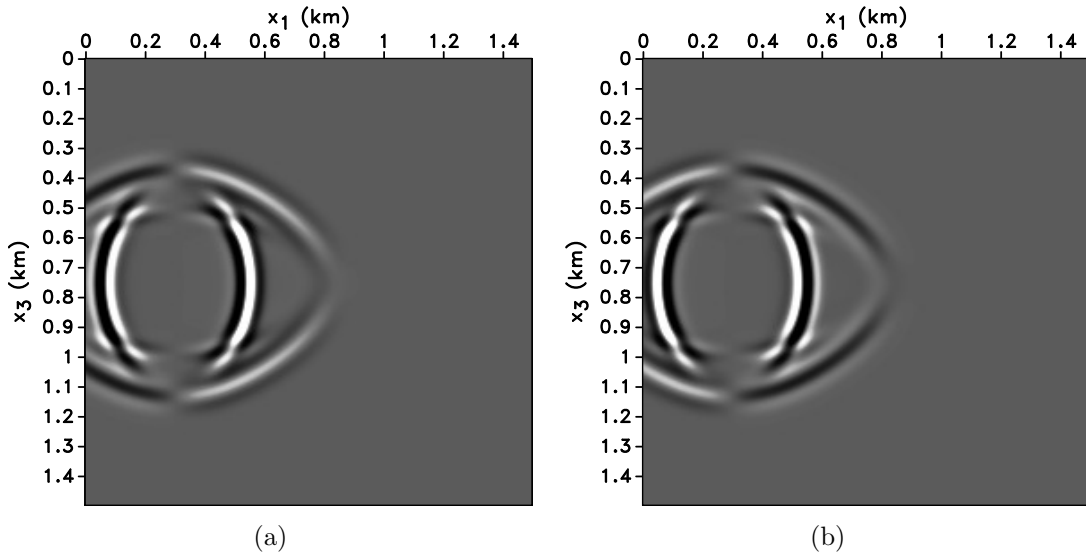


Figure 3.2: Snapshots of the vertical displacement for the model in Figure 3.1 at $t = 0.14$ s. (a) The observed wavefield produced by a dip-slip source with $\theta = 0^\circ$. (b) The predicted wavefield from a source with $\theta = 90^\circ$.

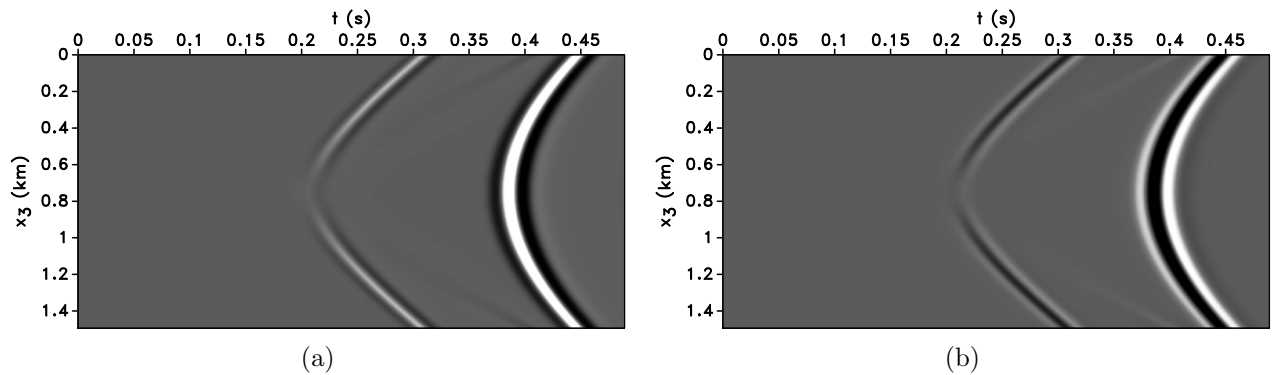


Figure 3.3: Vertical displacement of the (a) observed and (b) predicted data for the model in Figure 3.1.

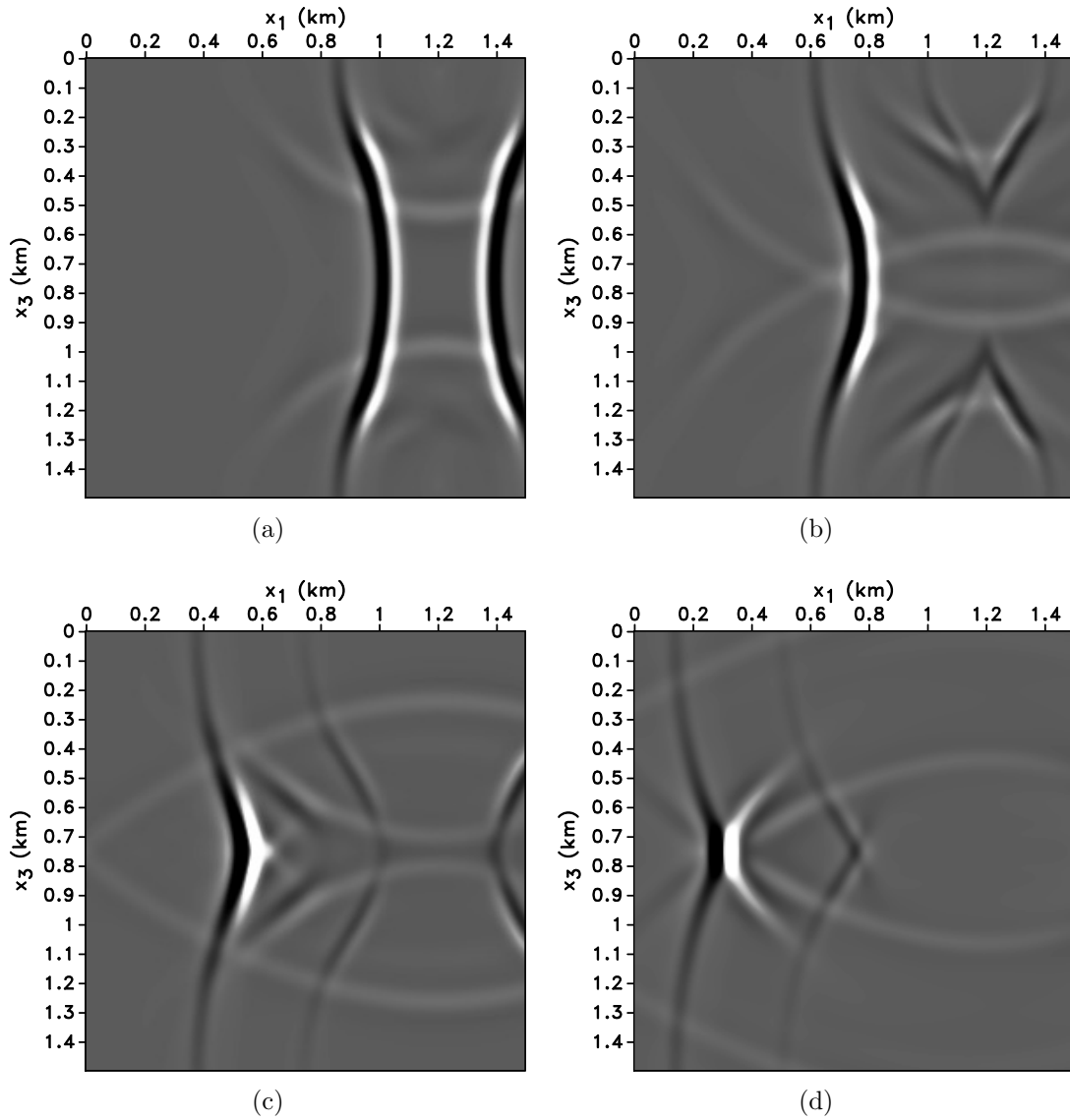


Figure 3.4: Snapshots of the vertical component of the adjoint wavefield for the model in Figure 3.1 at times (a) $t = 0.19$ s, (b) $t = 0.26$ s, (c) $t = 0.35$ s and (d) $t = 0.44$ s. The adjoint wavefield focuses at the actual and trial source locations (which are the same) on plot (d).

In the first experiment (Figure 3.1), the observed and initial predicted wavefields (Figure 3.2) and data (Figure 3.3) are generated for a single microseismic event recorded in a vertical “borehole” by receivers located at each grid point. Whereas the predicted field is excited by a horizontal dip-slip source ($\theta = 0^\circ$), the predicted field is computed with $\theta = 90^\circ$. Next, the adjoint source “injected” at the receiver locations is used to compute the adjoint wavefield (Figure 3.4). This wavefield focuses at the time $t = 0.44$ s near the actual source, where the model perturbation is located. The focusing time corresponds to the P-wave traveltimes along the raypath between the source and the receivers located at the end of the array.

After applying equations 3.2 – 3.4, the following derivatives for the five source parameters are obtained: $\partial\mathcal{F}/\partial M_{11} = 0.00038$, $\partial\mathcal{F}/\partial M_{13} = 1.28$, $\partial\mathcal{F}/\partial M_{33} = -0.0022$, $\partial\mathcal{F}/\partial x_1^s = 2.21$, $\partial\mathcal{F}/\partial x_3^s = -0.0039$, and $\partial\mathcal{F}/\partial t_0 = -0.82$. The sign of the derivatives (i.e., of the components of the gradient) defines the update direction in the model space, whereas their absolute values determine the magnitude of the update of the corresponding parameter. The units of the derivatives are not included here because we can compare only the derivatives for the same type of parameters (e.g., for the coordinates x_1^s and x_3^s).

The main contribution to the gradient comes from the focusing of the adjoint wavefield near the source location. It may look surprising that the derivatives for x_1^s , x_3^s , and t_0 are nonzero because the values of \mathbf{x}^s and t_0 for the actual and trial sources coincide. However, the derivatives for \mathbf{x}^s and t_0 depend on the components of \mathbf{M} , which deviate from the actual values (equations 3.3 and 3.4). Hence, to avoid cycle-skipping problems during the joint inversion for \mathbf{x}^s , t_0 , and \mathbf{M} , a good initial guess is needed for all three types of parameters.

The second test is performed for the three-layer VTI medium in Figure 3.5. The actual and trial models have the same source parameters as in the previous experiment. The data are generated by a source placed in the middle layer and recorded by receivers in a vertical “borehole.” The derivatives calculated using the adjoint-state method are $\partial\mathcal{F}/\partial M_{11} = 0.004$, $\partial\mathcal{F}/\partial M_{13} = 2.44$, $\partial\mathcal{F}/\partial M_{33} = -0.0044$, $\partial\mathcal{F}/\partial x_1^s = 0.82$, $\partial\mathcal{F}/\partial x_3^s = -0.0071$, and $\partial\mathcal{F}/\partial t_0 =$

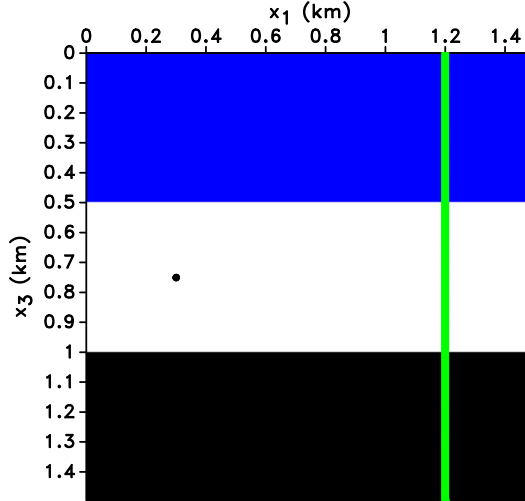


Figure 3.5: Three-layer VTI model used in the second experiment. The source-receiver geometry is the same as in Figure 3.1. The distance between receivers is 5 m. The parameters $\rho = 2 \text{ kg/m}^3$, $\epsilon = 0.4$, and $\delta = 0$ are the same in all three layers. The vertical velocities in the first layer are $V_{P0} = 4047 \text{ m/s}$ and $V_{S0} = 2638 \text{ m/s}$; for the second layer, $V_{P0} = 4169 \text{ m/s}$ and $V_{S0} = 2320 \text{ m/s}$; for the third layer, $V_{P0} = 4693 \text{ m/s}$ and $V_{S0} = 2682 \text{ m/s}$.

–0.21. These derivatives are similar to the ones obtained for the previous test because the tensor \mathbf{M} is perturbed in the same way for both cases. The layer boundaries, however, create a number of reflected and mode-converted waves that should make waveform inversion for source parameters better constrained.

For the third experiment, I keep the actual source at the same location as in the previous tests and use the homogeneous model from Figure 3.1. This time, the initial trial source is moved horizontally (Figure 3.6), which generates pronounced gradient contributions at both source locations. However, as mentioned above, the derivatives are required only at the trial source location.

The obtained derivatives are $\partial\mathcal{F}/\partial M_{11} = -0.00017$, $\partial\mathcal{F}/\partial M_{13} = -0.25$, $\partial\mathcal{F}/\partial M_{33} = 0.00033$, $\partial\mathcal{F}/\partial x_1^s = -4.28$, $\partial\mathcal{F}/\partial x_3^s = 0.0061$, and $\partial\mathcal{F}/\partial t_0 = 1.51$. Although the trial source has the correct moment tensor, the derivatives for M_{11} , M_{13} , and M_{33} do not vanish because the wavefield substantially changes with source location. The derivative for t_0 is also nonzero because moving the source creates traveltimes shifts similar to those due to a change in the origin time. Still, the inversion should be able to resolve the trade-off between \mathbf{x}^s and t_0

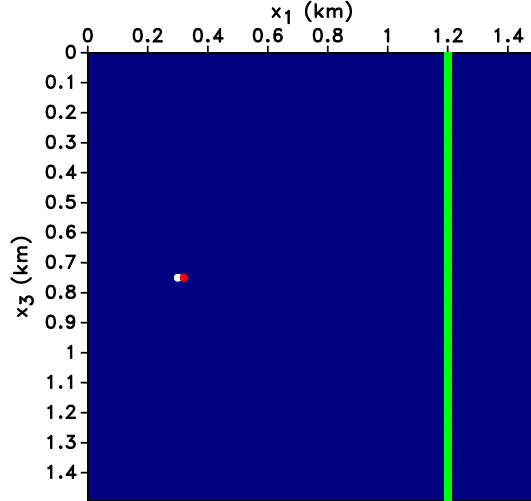


Figure 3.6: Actual source (white dot), trial source (red dot) and a vertical line of receivers (spacing is 6 m) embedded in a homogeneous VTI medium. The medium parameters are the same as in Figure 3.1. The actual source is located at $x_1 = 0.3$ km, $x_3 = 0.75$ km and the trial source is at $x_1 = 0.32$ km, $x_3 = 0.75$ km. The moment tensor for both sources corresponds to a horizontal ($\theta = 0^\circ$) dip-slip fault with $\Sigma \bar{u} = 1 \text{ m}^3$.

because they influence the traveltimes in a different fashion (see discussion in chapter 4).

The large value of $\partial\mathcal{F}/\partial x_1^s$ compared to $\partial\mathcal{F}/\partial x_3^s$ correctly indicates that the trial horizontal source coordinate x_1^s should be updated more significantly than x_3^s . The negative sign of $\partial\mathcal{F}/\partial x_1^s$ will lead to a smaller value of x_1^s for the next iteration of inversion, so that the source will move toward its actual position ($x_1 = 0.3$ km.)

The last experiment demonstrates another potential application of the adjoint wavefield. The model includes two actual sources with the same tensor \mathbf{M} and origin time t_0 that generate the wavefield $\mathbf{u}(\mathbf{x}, t)$ (Figure 3.7). However, I assume that the data \mathbf{d}_{obs} are produced by a single event and specify a single trial source. In general, the adjoint wavefield \mathbf{u}^\dagger is expected to focus at two different locations, corresponding approximately to the actual and trial source position. Instead, the adjoint wavefield actually focuses at three locations (Figure 3.8), which helps identify the second source missing in the trial model.

In addition to finding “hidden sources,” the field \mathbf{u}^\dagger can be used to improve the initial trial source position because the adjoint wavefield focuses (for the correct velocity model) near the actual source location. This starting source position can be later refined by WI.

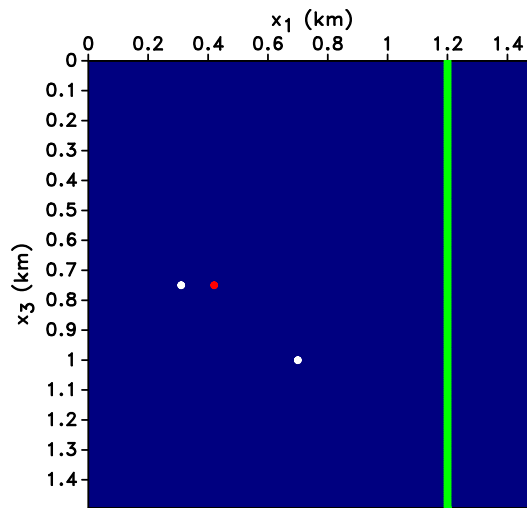


Figure 3.7: Two actual sources (white dots), a trial source (red dot), and a vertical line of receivers (the spacing is 6 m) embedded in a homogeneous VTI medium. The medium parameters are the same as in Figure 3.1. The actual sources are located at $x_1 = 0.3$ km, $x_3 = 0.75$ km, and $x_1 = 0.7$ km, $x_3 = 1$ km; the trial source is at $x_1 = 0.42$ km, $x_3 = 0.75$ km. The moment tensor for all three sources corresponds to a horizontal ($\theta = 0^\circ$) dip-slip fault with $\Sigma \bar{u} = 1 \text{ m}^3$.

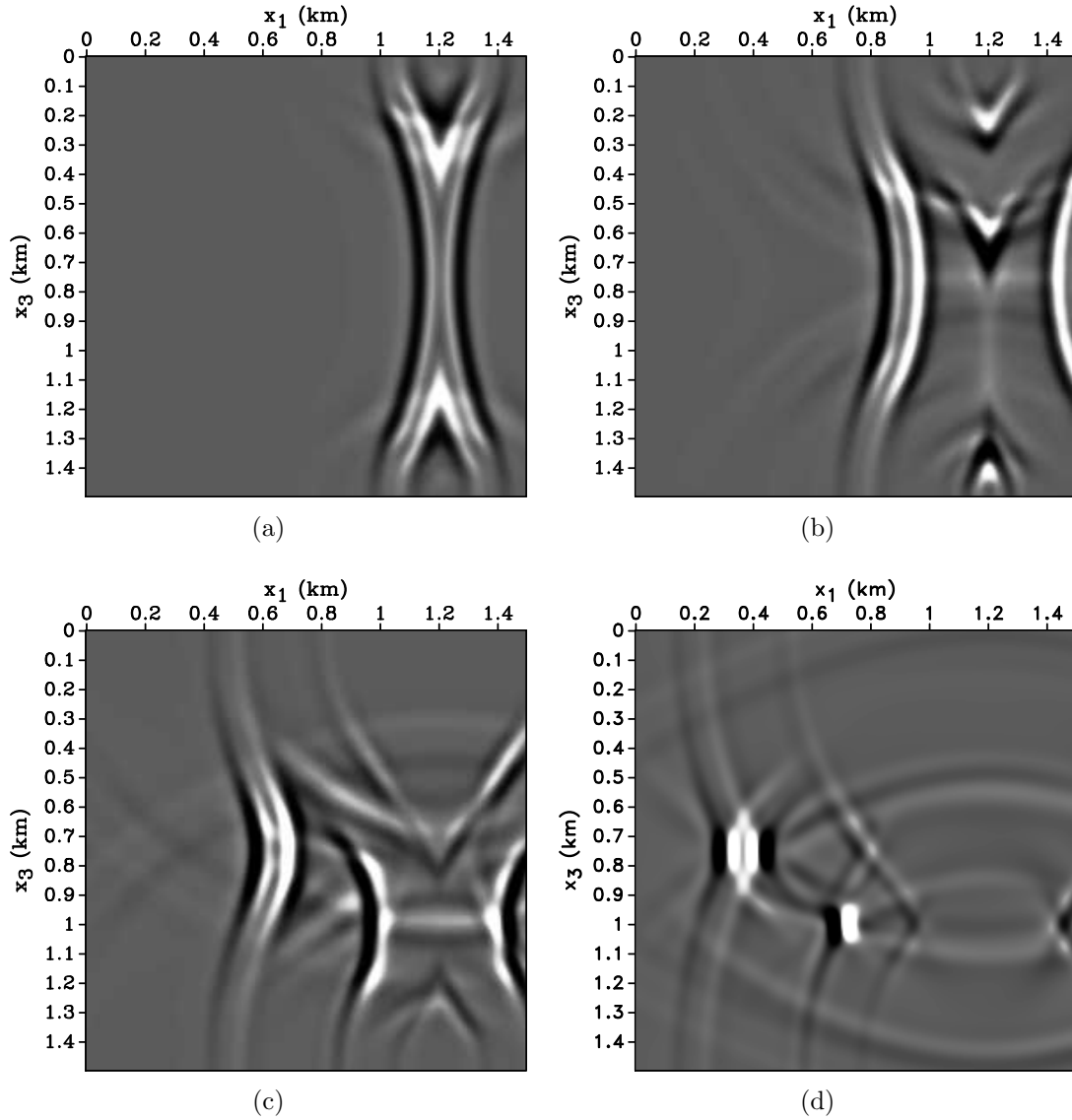


Figure 3.8: Snapshots of the vertical component of the adjoint wavefield for the model in Figure 3.7 at times (a) $t = 0.12$ s, (b) $t = 0.23$ s, (c) $t = 0.33$ s, and (d) $t = 0.44$ s. The adjoint wavefield on plot (d) focuses at both actual source locations and at the trial source location.

CHAPTER 4

WAVEFORM INVERSION FOR MICROSEISMIC SOURCE PARAMETERS

In this chapter, I discuss application of WI to the estimation of microseismic source parameters. The gradient is computed from the adjoint-state method as described in Chapter 3. The synthetic tests illustrate how the outcome of the inversion changes with model assumptions and how the choice of a line-search method influences the inversion results.

4.1 Implementation

The model parameters have different units, and local minimization of $\mathcal{F}(\mathbf{m})$ could be performed for each parameter class separately. However, it is preferable to implement simultaneous inversion for \mathbf{x}^s , t_0 , and \mathbf{M} which could be done using the nondimensionalization approach suggested by Kim et al. (2011). This approach eliminates the difference between the units of different parameters classes, which makes possible simultaneous parameter updating and avoids the additional cost of multidirectional optimization. At the first iteration, the following scaling coefficients σ are defined for each parameter class:

$$\sigma_{\mathbf{x}^s} = \beta_{\mathbf{x}^s} \frac{1}{\sqrt{g_{x_1^s}^2 + g_{x_3^s}^2}}, \quad (4.1)$$

$$\sigma_{t_0} = \beta_{t_0} \frac{1}{|g_{t_0}|}, \quad (4.2)$$

$$\sigma_{\mathbf{M}} = \beta_{\mathbf{M}} \frac{1}{\sqrt{g_{M_{11}}^2 + g_{M_{13}}^2 + g_{M_{33}}^2}}, \quad (4.3)$$

where the quantities $\beta_{\mathbf{x}^s}$, β_{t_0} , and $\beta_{\mathbf{M}}$ are scaling factors that ensure that each parameter class gives a comparable contribution to the gradient. These factors may be different for each experiment and can be determined, for instance, by evaluating the change in the gradient produced by β_c (c indicates the parameter class) between the first and second iteration. The

“nondimensionalized” model parameters are:

$$\hat{\mathbf{m}}_{\mathbf{c}} = \frac{\mathbf{m}_{\mathbf{c}}}{\sigma_{\mathbf{c}}} . \quad (4.4)$$

The gradient becomes dimensionless after the following scaling:

$$\hat{\mathbf{g}}_{\mathbf{c}} = \mathbf{g}_{\mathbf{c}} \sigma_{\mathbf{c}} . \quad (4.5)$$

As discussed in more detail below, the inverse problem is nonlinear, and it is solved here using an iterative local gradient-descent scheme. Suppose the model \mathbf{m}^k is obtained after $k - 1$ iterations of the inversion algorithm. First, the forward simulation is performed to generate the predicted data $\mathbf{d}_{\text{pre}}^k(\mathbf{m}^k)$, which allows us to compute the objective function \mathcal{F}^k . Then, the adjoint simulation to calculate the gradient \mathbf{g}^k is carried out using equations 3.3 – 3.2. The next step is nondimensionalization of the model parameters (equation 4.4) and scaling of the gradient (equation 4.5). Note that the scaling coefficients are computed at the first iteration and kept constant during the inversion. Because the nondimensionalized model parameters have the same units (those of \mathcal{F}) and the scaled gradient is dimensionless, the three classes of parameters can be updated simultaneously using a certain step length α :

$$\hat{\mathbf{m}}^{k+1} = \hat{\mathbf{m}}^k + \alpha^k \hat{\mathbf{g}}^k . \quad (4.6)$$

Assuming that $\hat{\mathbf{m}}^k$ is located within the basin that contains the global minimum of \mathcal{F} , the step length should be sufficiently small to ensure that $\hat{\mathbf{m}}^{k+1}$ stays within this basin. After the update, the parameters have to be “dimensionalized” again so that they can be used as inputs for the forward modeling in the next iteration:

$$\mathbf{m}_{\mathbf{c}}^{k+1} = \hat{\mathbf{m}}_{\mathbf{c}}^{k+1} \sigma_{\mathbf{c}} . \quad (4.7)$$

4.2 Properties of the inverse problem

Estimating the moment tensor \mathbf{M} of an earthquake from seismic amplitudes is a linear inverse problem. However, simultaneous inversion for \mathbf{x}^{s} , t_0 and \mathbf{M} is nonlinear because the recorded data depend on \mathbf{x}^{s} and t_0 in a nonlinear fashion. The joint inversion for \mathbf{x}^{s} , t_0 , and \mathbf{M} involves complications typical for velocity estimation using WI. For example, cycle-

skipping can occur if the trial model is too far from the actual one or if the step length α used in model updating is too large. In particular, the trial source should be within about one-half of the predominant wavelength from the actual source location, which is achievable using traveltimes inversion methods.

Figure 4.1 shows the variation of the normalized objective function with the coordinates \mathbf{x}^s and time t_0 . To ensure convergence to the actual values, the trial model should lie within the basin that contains the global minimum. If the inversion involves simultaneous estimation of x_1^s , x_3^s , and t_0 , the basin containing the global minimum in the plots of Figure 4.1 becomes more narrow, which increases the risk of cycle skipping.

4.3 Synthetic tests with a constant step length

Here, I present synthetic tests of the WI algorithm for a homogeneous VTI medium and a stack of horizontal VTI layers. In all experiments, the observed data are generated by a single microseismic event recorded by a vertical array of closely spaced receivers. In this section, the results are obtained using a constant step length for parameter updating.

In the first experiment, I invert for the parameters x_1^s , x_3^s , M_{11} , M_{13} , and M_{33} with the origin time t_0 fixed at the actual value (Figure 4.2). Because the medium is homogeneous, the wavefield is composed just of the direct P- and SV-waves. The objective function becomes practically negligible after about 10 iterations (Figure 4.3). The source coordinates (Figure 4.4) and moment tensor (Figure 4.5) are estimated with high accuracy, with the errors in x_1^s and x_3^s on the order of centimeters. Note that the algorithm was able to resolve the moment tensor \mathbf{M} , although the data were acquired in a single vertical borehole. The pronounced variations in \mathbf{M} during the initial iterations are due to the incorrect position of the source, which produces large changes in the amplitudes of the P- and SV-waves.

In the second test, the origin time t_0 is perturbed, while the location \mathbf{x}^s is fixed at the correct value (Figure 4.6). The tensor \mathbf{M} is perturbed in the same way as in the previous example. The rate of the decrease of the objective function (Figure 4.7) is similar to that in the previous test. The direct P and SV arrivals recorded in a single borehole provide

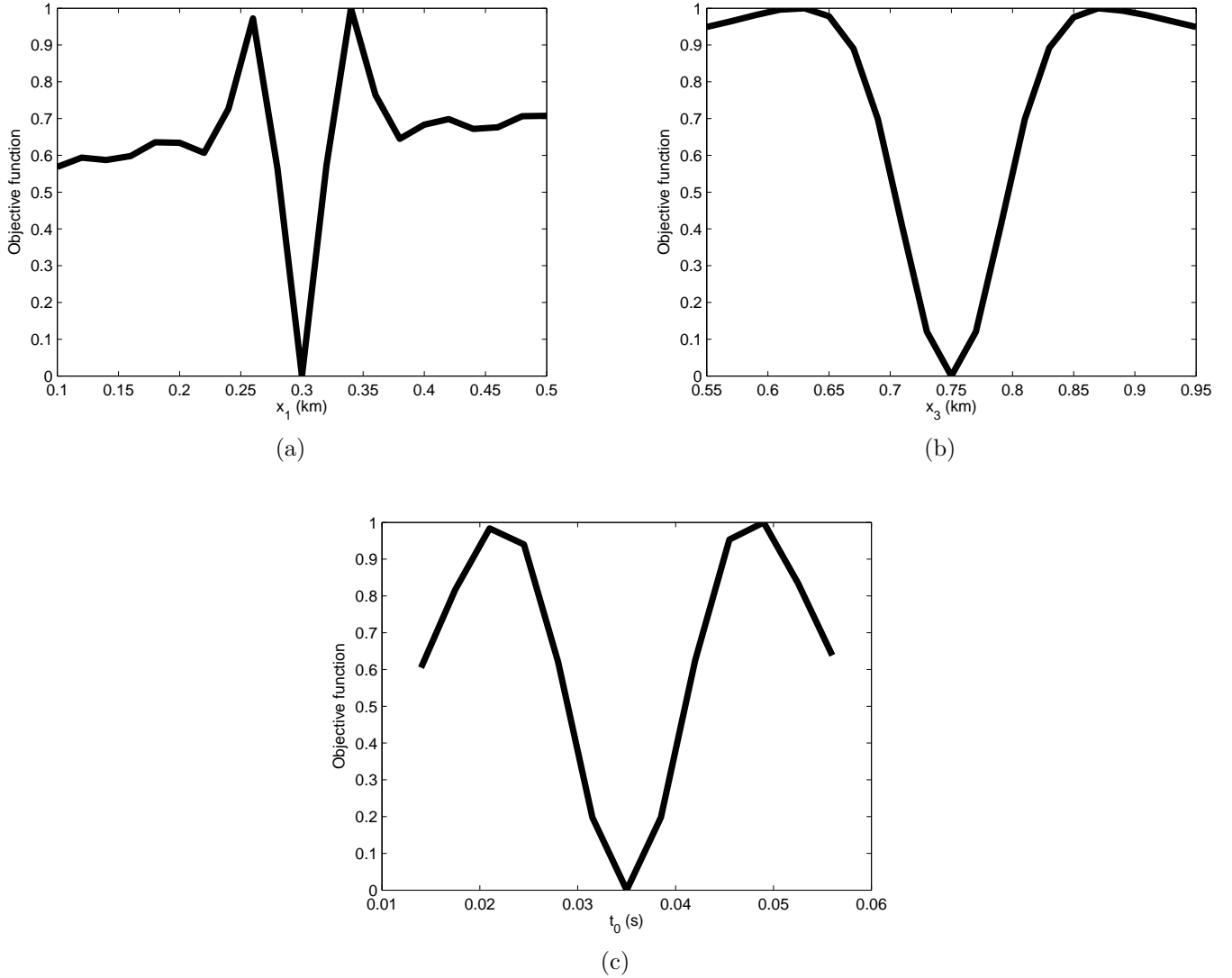


Figure 4.1: Dependence of the objective function $\mathcal{F}(\mathbf{m})$ on the trial source parameters (a) x_1^s , (b) x_3^s , and (c) t_0 for a homogeneous VTI model. The global minimum coincides with the actual parameter value. The components of the tensor \mathbf{M} are fixed at the actual values. The medium parameters are $\rho = 2 \text{ g/cm}^3$, $V_{P0} = 4047 \text{ m/s}$, $V_{S0} = 2638 \text{ m/s}$, $\epsilon = 0.4$, and $\delta = 0$.

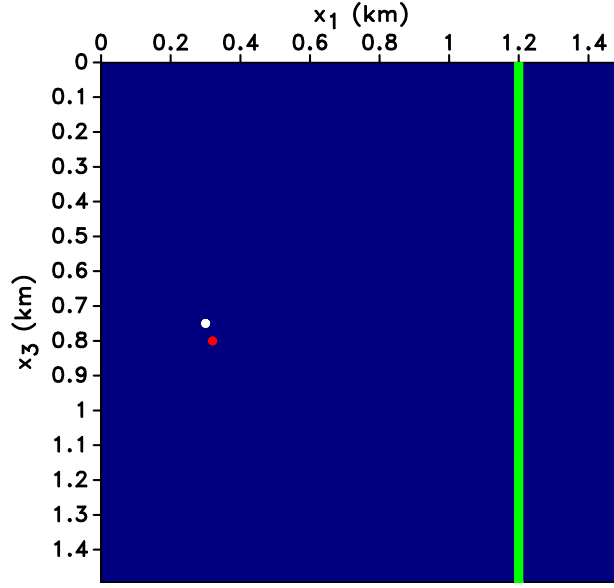


Figure 4.2: Actual source (white dot), trial source (red dot) and a vertical line of receivers (spacing is 6 m) embedded in a homogeneous VTI medium. The medium parameters are $\rho = 2 \text{ g/cm}^3$, $V_{P0} = 4047 \text{ m/s}$, $V_{S0} = 2638 \text{ m/s}$, $\epsilon = 0.4$, and $\delta = 0$. The actual source is located at $x_1 = 0.3 \text{ km}$ and $x_3 = 0.75 \text{ km}$ with $\theta = 0^\circ$ (see equations 2.9 – 2.11). For the trial source, $x_1 = 0.32 \text{ km}$, $x_3 = 0.8 \text{ km}$, and $\theta = 15^\circ$. Both events occur at the same time ($t_0 = 0.049 \text{ s}$) and have the same $\Sigma \bar{u} = 1 \text{ m}^3$.

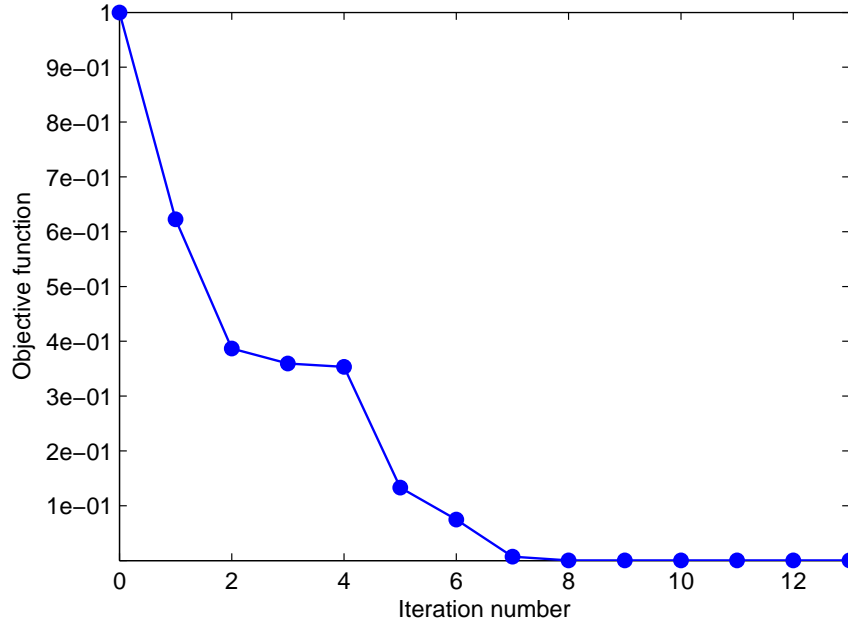


Figure 4.3: Change of the normalized objective function $\mathcal{F}(\mathbf{m})$ with iterations for the model in Figure 4.2.

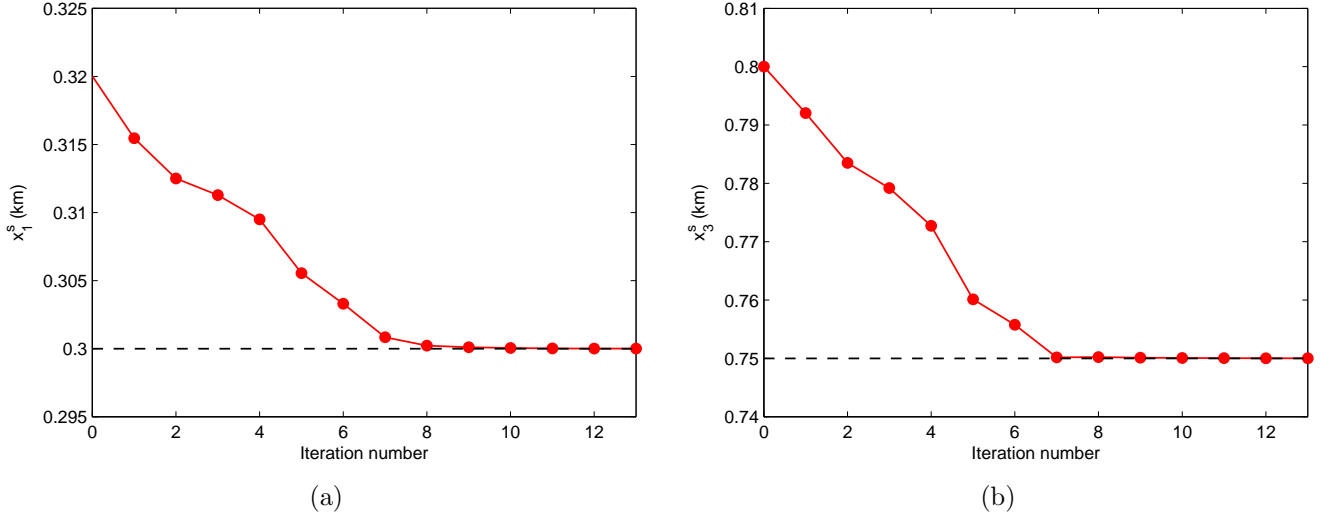


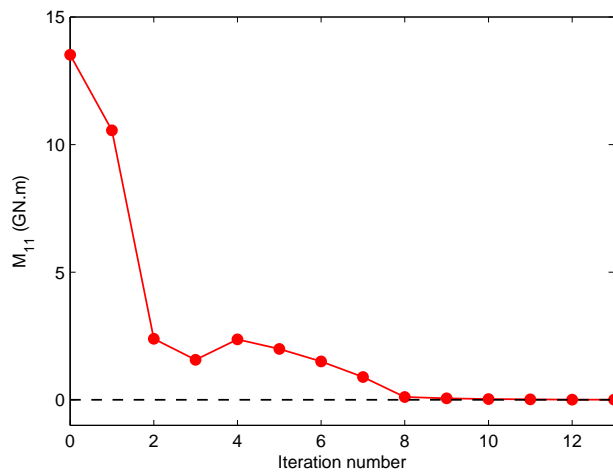
Figure 4.4: Change of the source coordinates (a) x_1^s and (b) x_3^s with iterations for the model in Figure 4.2. The actual values are marked by dashed lines.

sufficient information to constrain the parameters t_0 (Figure 4.8) and \mathbf{M} (Figure 4.9).

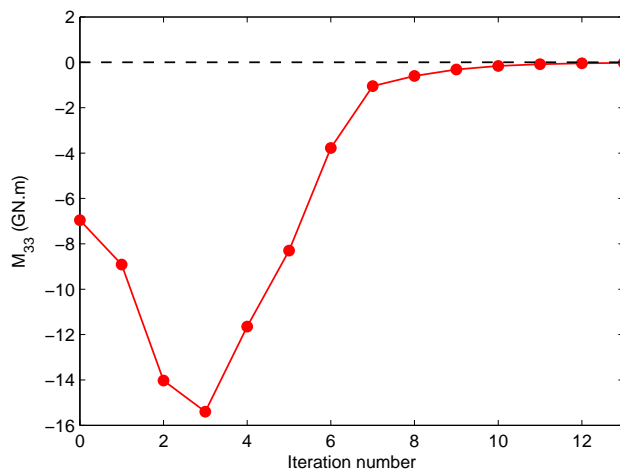
Next, I use the five-layer model in Figure 4.10 with perturbed \mathbf{x}^s and \mathbf{M} and assume that all source parameters (\mathbf{x}^s , t_0 , and \mathbf{M}) are unknown. The multiple layers in this model produce numerous scattered waves, which help constrain the source location. Although the origin time t_0 for the actual and trial sources coincides, it varies with iterations as WI tries to match the observed and predicted data.

In theory, moving the source vertically shifts the apex of the P- and S-wave moveouts up or down, with the depth of the apex determining the vertical coordinate x_3^s . Also, variations in the horizontal distance between the source and the receiver array change the difference between the S- and P-wave traveltimes. In contrast, changing the origin time simply shifts the P- and S-wave moveouts along the time axis without moving them in depth or altering their difference. Therefore, the parameters \mathbf{x}^s and t_0 influence the traveltimes in a different way, which should preclude a trade-off between them.

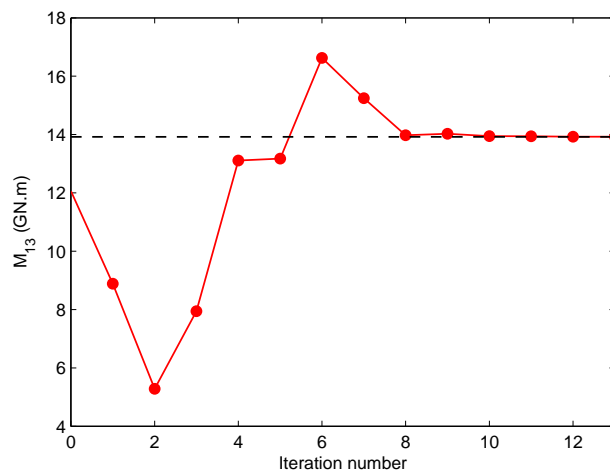
Even if \mathbf{x}^s and t_0 are unknown, the objective function can be reduced after nine iterations to 1.4×10^{-4} (Figure 4.11); in the previous example it was reduced more significantly to 8.6×10^{-5} (Figure 4.3). Also, the obtained horizontal source coordinate x_1^s (Figure 4.12) and



(a)



(b)



(c)

Figure 4.5: Change of the moment-tensor elements (a) M_{11} , (b) M_{33} , and (c) M_{13} with iterations for the model in Figure 4.2. The actual values are marked by dashed lines.

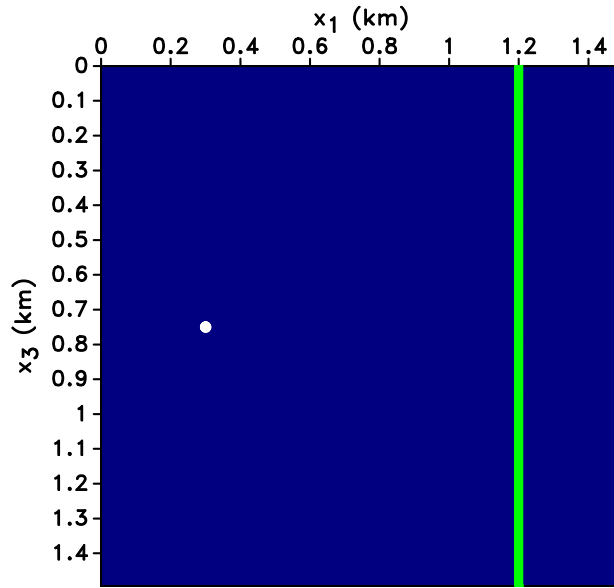


Figure 4.6: Source (white dot) and a vertical line of receivers (spacing is 6 m) embedded in a homogeneous VTI medium. The medium parameters are the same as in Figure 4.2. The location of the actual and trial sources is the same: $x_1 = 0.3$ km and $x_3 = 0.75$ km, as well as $\Sigma \bar{u} = 1 \text{ m}^3$. For the actual source, $t_0 = 0.049$ s and $\theta = 0^\circ$, for the trial source, $t_0 = 0.042$ s and $\theta = 15^\circ$.

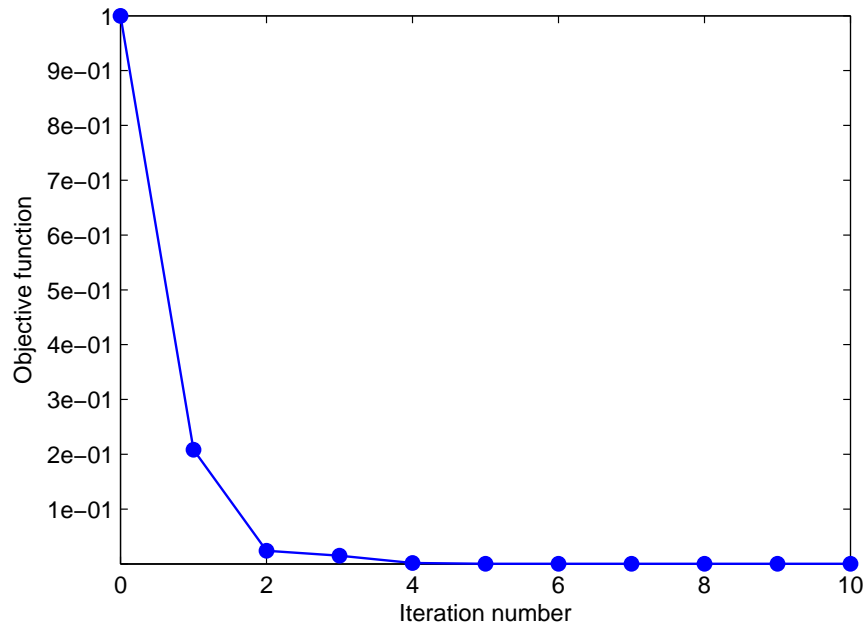


Figure 4.7: Change of the normalized objective function $\mathcal{F}(\mathbf{m})$ with iterations for the model in Figure 4.6.

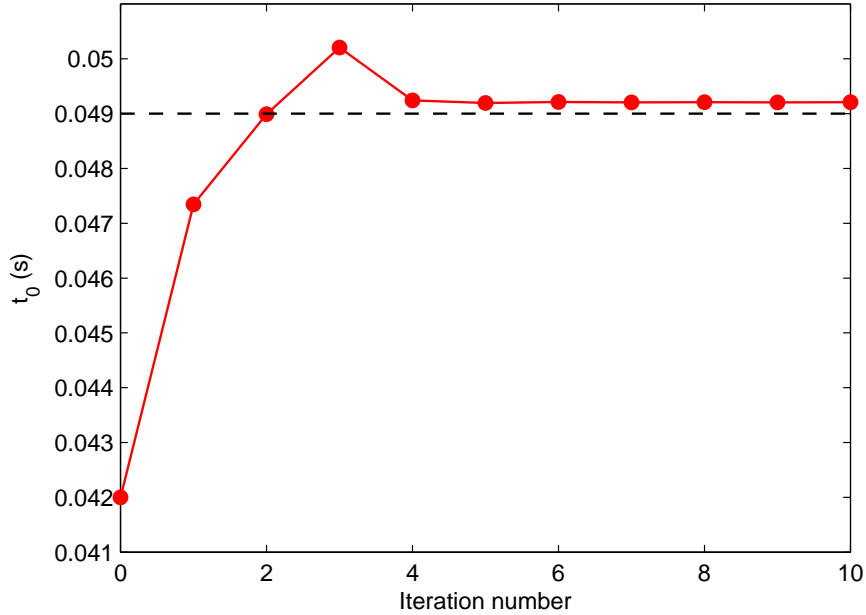
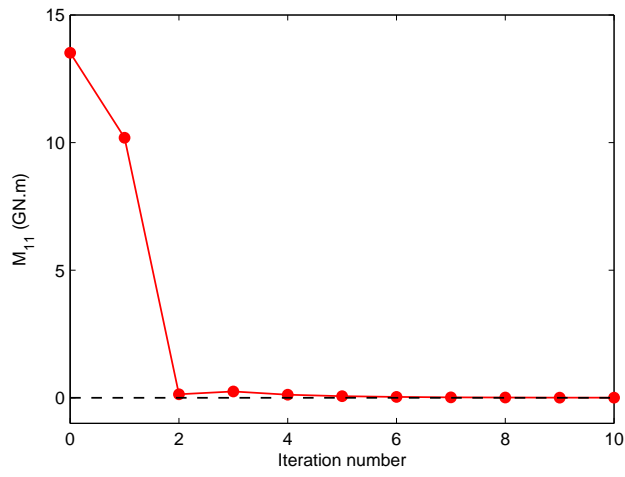


Figure 4.8: Change of the origin time t_0 with iterations for the model in Figure 4.6.

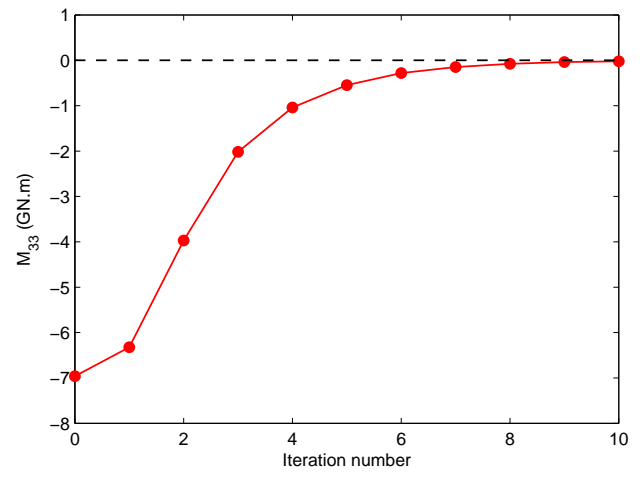
time t_0 (Figure 4.13) are slightly distorted. This is because the P- and SV-traveltime shifts produced by further perturbations in the source location and origin time become too small to rapidly guide the inversion toward the actual model.

In the fourth experiment I use the model in Figure 4.10, but invert only for \mathbf{M} and \mathbf{x}^s , with the origin time t_0 fixed at the correct value. The objective function rapidly decays with iterations (Figure 4.14), and the obtained source location is practically exact (Figure 4.15). Also, the inversion accurately estimates all three elements of the tensor \mathbf{M} (Figure 4.16).

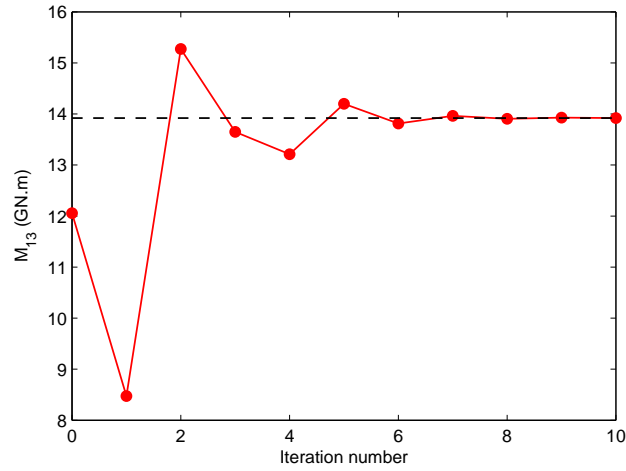
The previous tests assumed the correct velocity model for WI. The next example helps evaluate the influence of velocity errors on the inversion results by using a distorted anisotropy coefficient ϵ for the homogeneous VTI model in Figure 4.2. The algorithm estimates the parameters \mathbf{x}^s and \mathbf{M} , whereas the origin time t_0 is fixed at the actual value. In particular, an error in ϵ changes the P-wave horizontal velocity V_{hor} , which should influence estimation of the horizontal source coordinate x_1^s . After a fast initial decrease, the objective function flattens out (Figure 4.17) at a larger value than that in Figure 4.3. Still, errors in the source coordinates are relatively small (about 5 m for x_1^s) as shown in Figure 4.18, and the elements



(a)



(b)



(c)

Figure 4.9: Change of the moment-tensor elements (a) M_{11} , (b) M_{33} , and (c) M_{13} with iterations for the model in Figure 4.6.

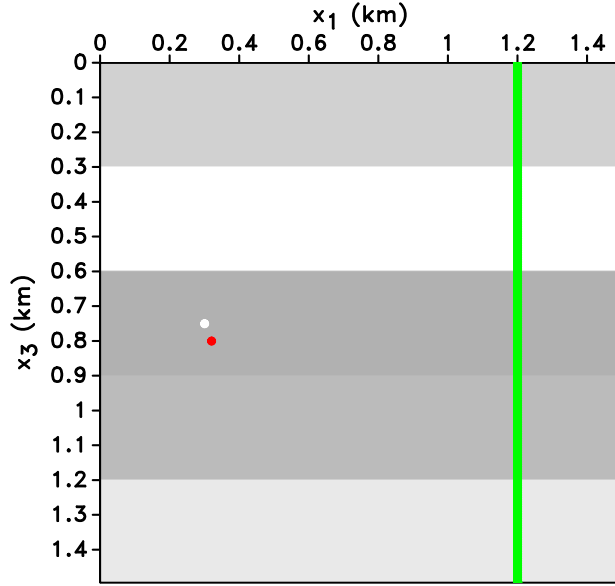


Figure 4.10: Actual (white dot) and trial (red dot) sources and a vertical receiver array in a five-layer VTI model. The receiver geometry is the same as in Figure 4.2. The parameters $\rho = 2 \text{ kg/m}^3$, $\epsilon = 0.4$, and $\delta = 0$ are the same in all five layers. The vertical velocities in the top layer are $V_{P0} = 4419 \text{ m/s}$ and $V_{S0} = 2645 \text{ m/s}$; for the second layer, $V_{P0} = 4956 \text{ m/s}$ and $V_{S0} = 2424 \text{ m/s}$; for the third layer, $V_{P0} = 4048 \text{ m/s}$ and $V_{S0} = 2638 \text{ m/s}$; for the fourth layer, $V_{P0} = 4170 \text{ m/s}$ and $V_{S0} = 2320 \text{ m/s}$; for the fifth layer, $V_{P0} = 4694 \text{ m/s}$ and $V_{S0} = 2682 \text{ m/s}$. The actual source is located at $x_1 = 0.3 \text{ km}$ and $x_3 = 0.75 \text{ km}$ with $\theta = 0^\circ$. The trial source is located at $x_1 = 0.32 \text{ km}$ and $x_3 = 0.8 \text{ km}$ with $\theta = 15^\circ$. Both events occur at the same time ($t_0 = 0.035 \text{ s}$) and have the same $\Sigma \bar{u} = 1 \text{ m}^3$.

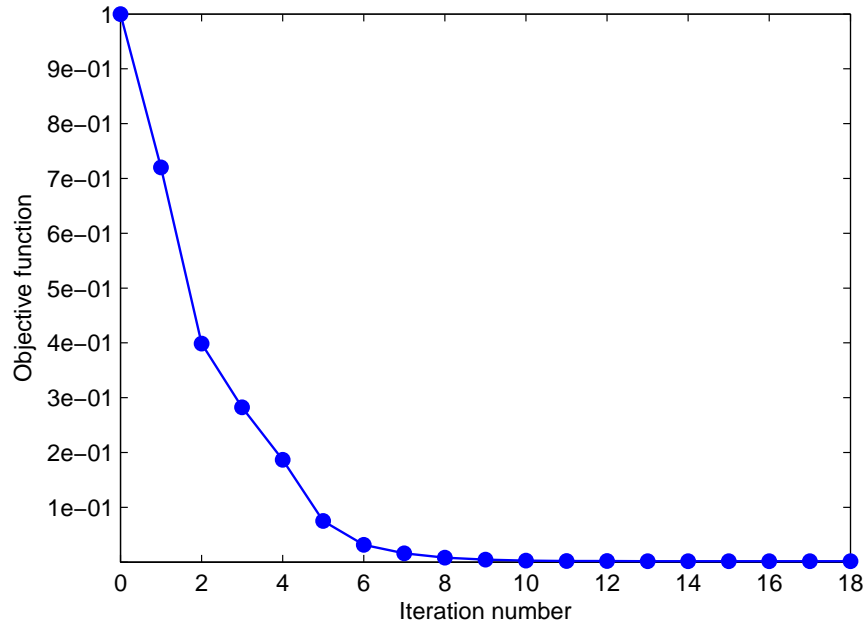


Figure 4.11: Change of the normalized objective function $\mathcal{F}(\mathbf{m})$ with iterations for the model in Figure 4.10. All source parameters are unknown.

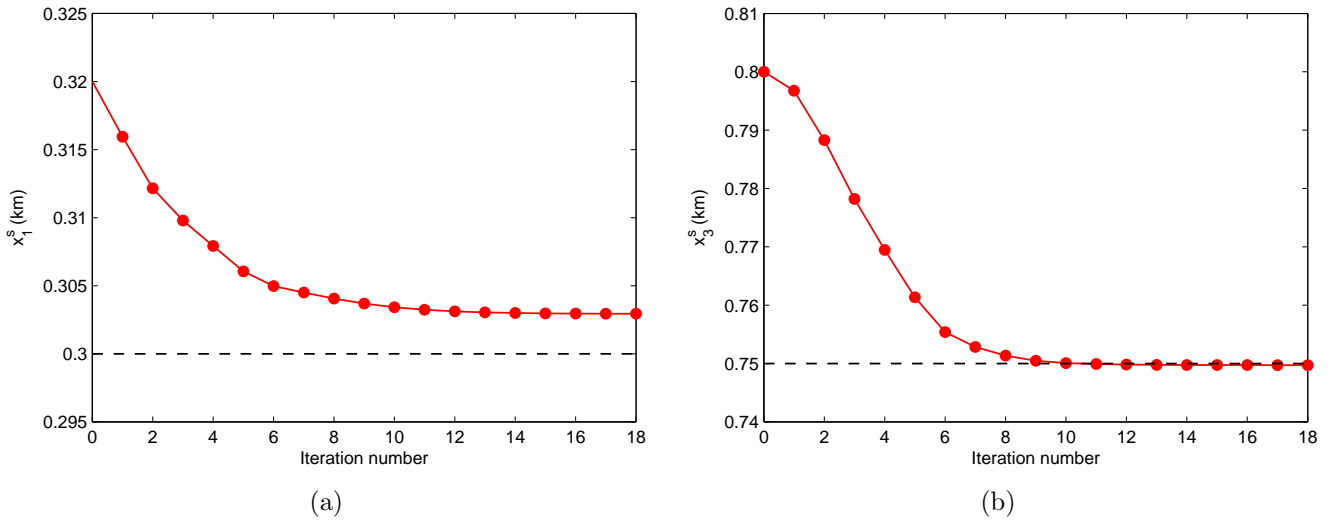


Figure 4.12: Change of the source coordinates (a) x_1^s and (b) x_3^s with iterations for the model in Figure 4.10.

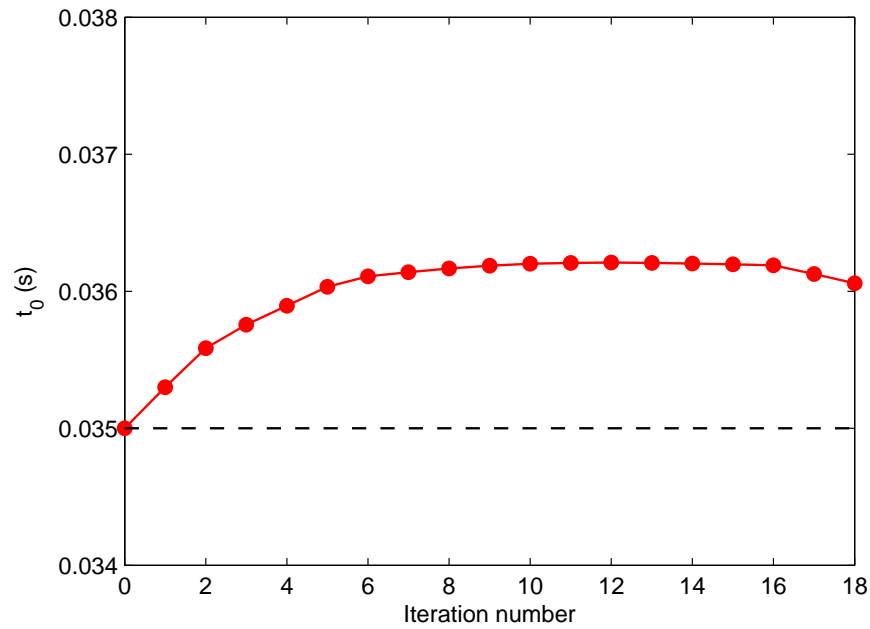


Figure 4.13: Change of the origin time t_0 with iterations for the model in Figure 4.10.

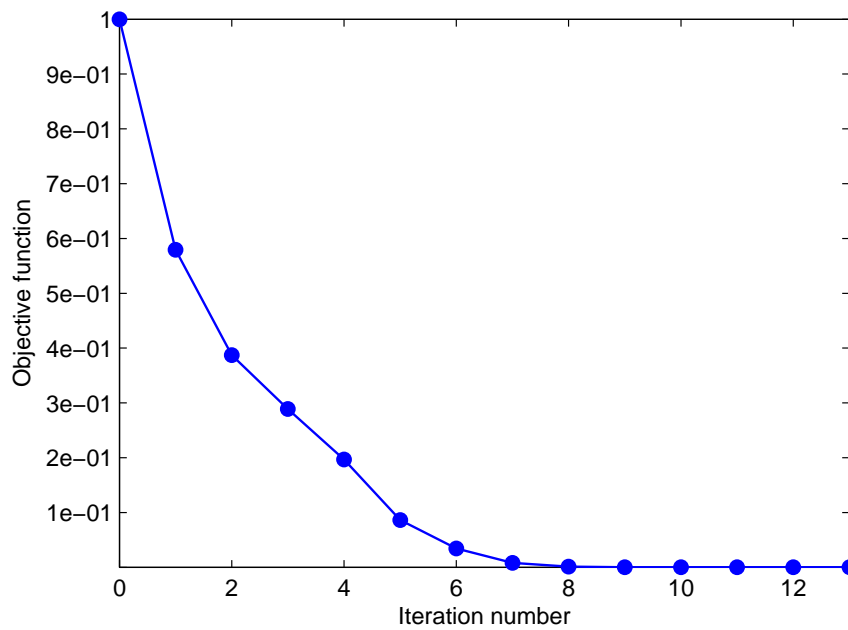


Figure 4.14: Change of the normalized objective function $\mathcal{F}(\mathbf{m})$ with iterations for the model in Figure 4.10. The origin time t_0 is fixed at the correct value.

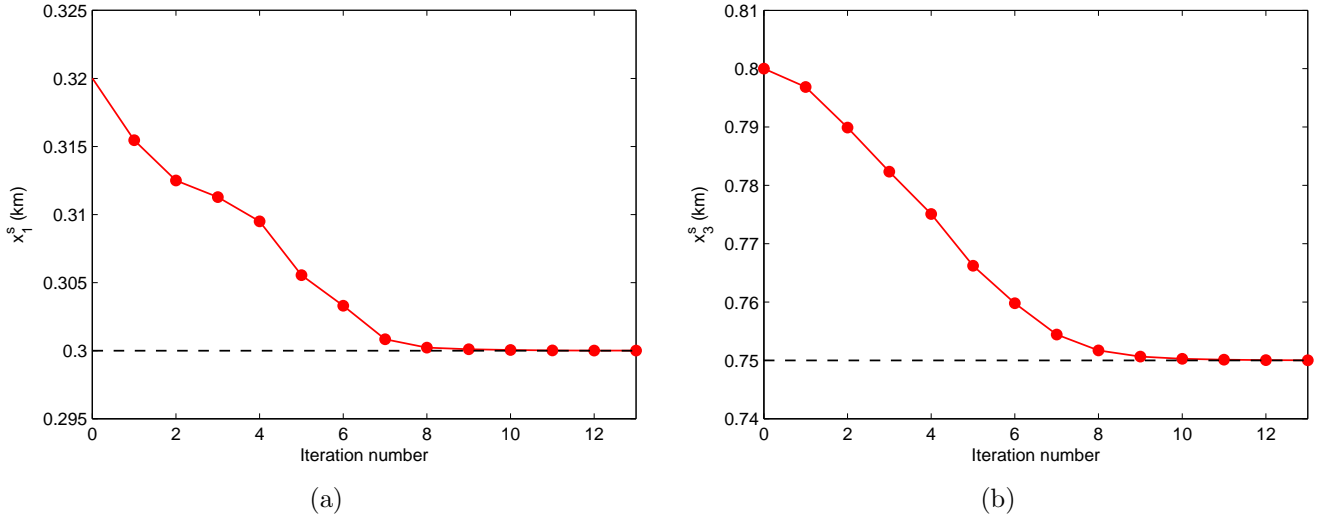
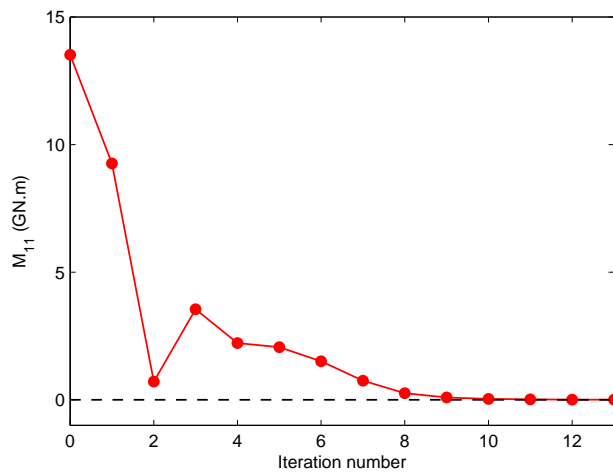


Figure 4.15: Change of the source coordinates (a) x_1^s and (b) x_3^s with iterations for the model in Figure 4.10. The origin time t_0 is fixed at the correct value.

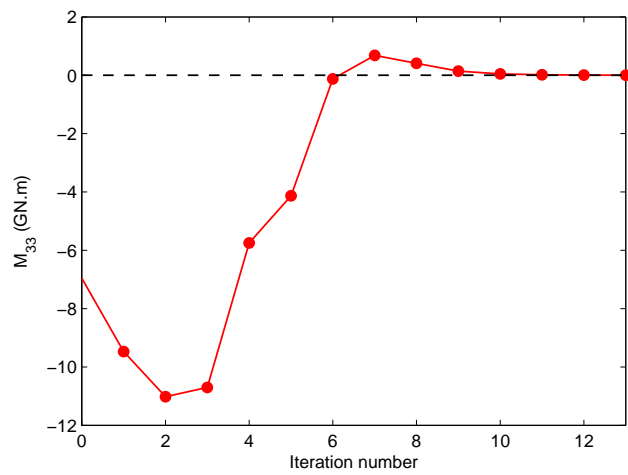
M_{11} and M_{33} of the moment tensor are also recovered with high accuracy Figure 4.19. However, there is a more significant error (over 20%) in the element M_{13} , which is most sensitive to the quality of waveform matching.

The goal of the final test is to evaluate the influence of noise in the input data on the inversion results. We use the homogeneous VTI model from Figure 4.2 and add random Gaussian noise in the frequency band of the observed data with the variance equal to 0.07% of the maximum amplitude. The noise does not mask the arrivals but creates significant distortions in the seismogram (Figure 4.20). The inversion algorithm estimates \mathbf{x}^s and \mathbf{M} , whereas the origin time t_0 is fixed at the actual value; the results of this test with noise-free data are shown in Figures 4.3 – 4.5. The objective function (Figure 4.21) is not monotonic and flattens out at a larger value than that in Figure 4.3, as expected for noise-contaminated data.

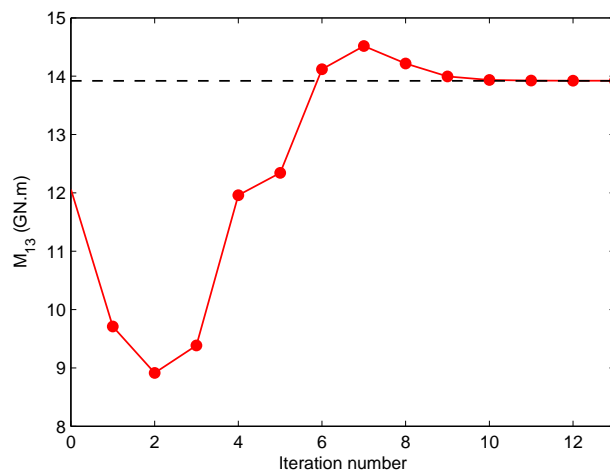
Still, despite the substantial magnitude of noise, the errors in the estimated source coordinates (Figure 4.22) and the elements of the tensor \mathbf{M} (Figure 4.23) are relatively small. The only noticeably distorted parameter is the tensor element M_{13} , for which the error is about 16%. Because the noise influences mainly the amplitudes, one would expect it to



(a)



(b)



(c)

Figure 4.16: Change of the moment-tensor elements (a) M_{11} , (b) M_{33} , and (c) M_{13} with iterations for the model in Figure 4.10. The origin time t_0 is fixed at the correct value.

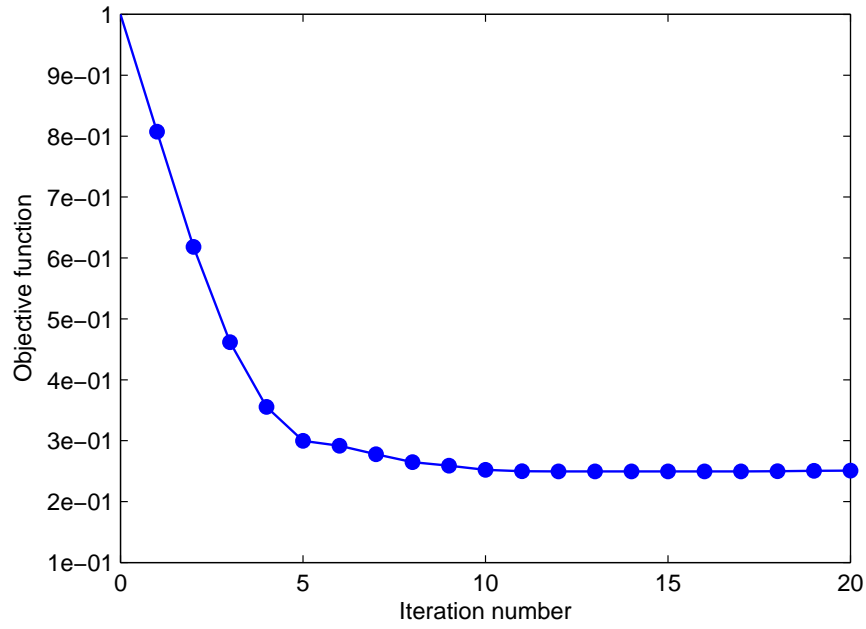


Figure 4.17: Change of the normalized objective function $\mathcal{F}(\mathbf{m})$ with iterations for the model in Figure 4.2. The inversion is performed with an incorrect value of ϵ ($\epsilon = 0.3$ instead of the actual 0.4). The rest of the VTI parameters are unchanged.

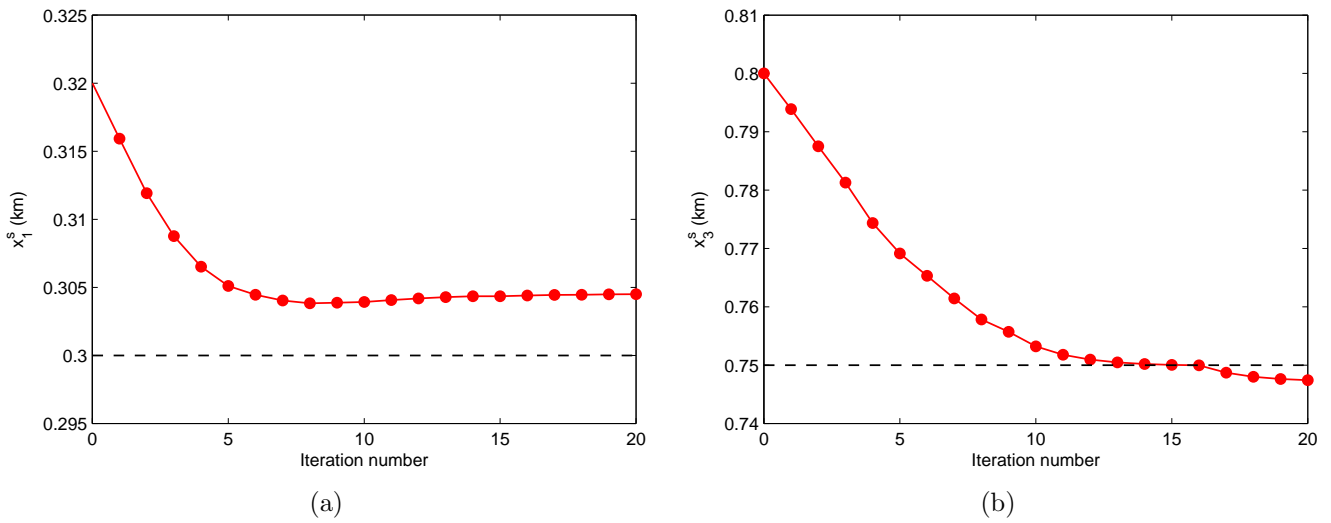
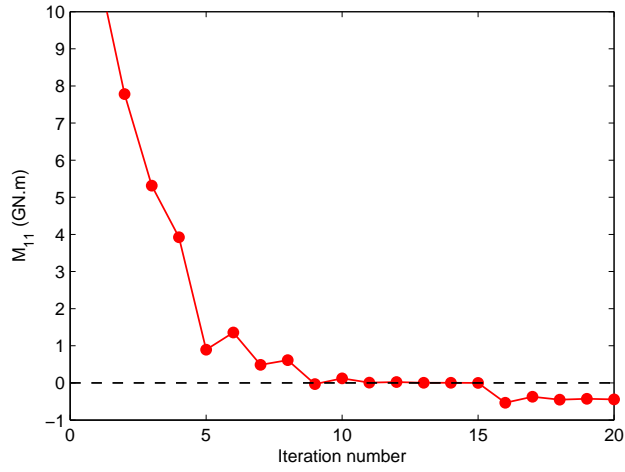
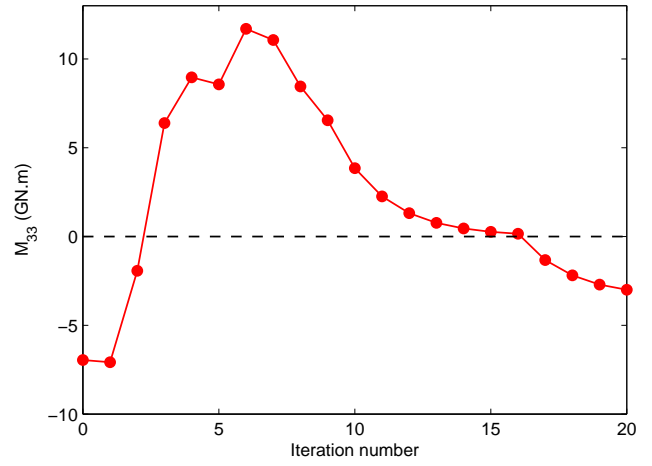


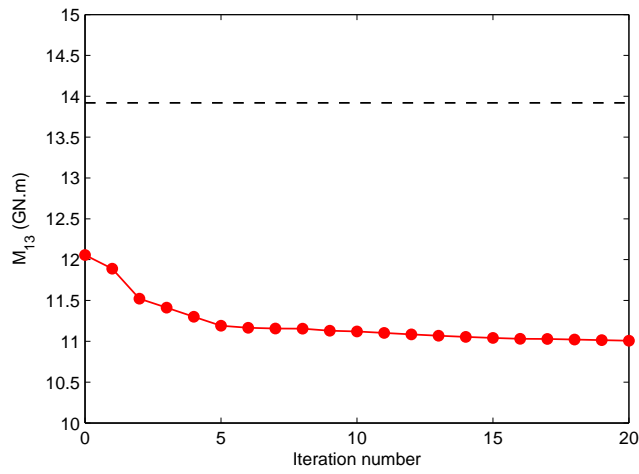
Figure 4.18: Change of the source coordinates (a) x_1^s and (b) x_3^s with iterations for the model in Figure 4.2. The inversion uses $\epsilon = 0.3$ instead of the actual $\epsilon = 0.4$.



(a)



(b)



(c)

Figure 4.19: Change of the moment-tensor elements (a) M_{11} , (b) M_{33} , and (c) M_{13} with iterations for the model in Figure 4.2. The inversion uses $\epsilon = 0.3$ instead of the actual $\epsilon = 0.4$.

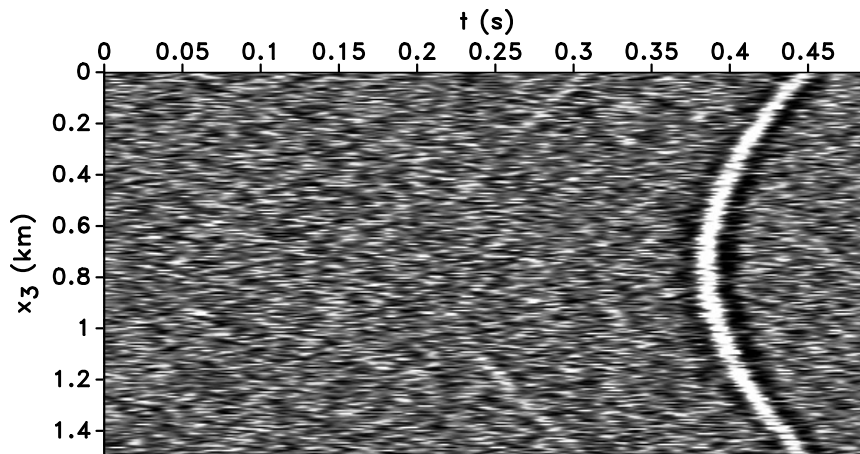


Figure 4.20: Vertical displacement of the observed data contaminated with Gaussian noise for the model in Figure 4.2. The noise has the same frequency band as the data and the variance is equal to 0.07% of the maximum amplitude.

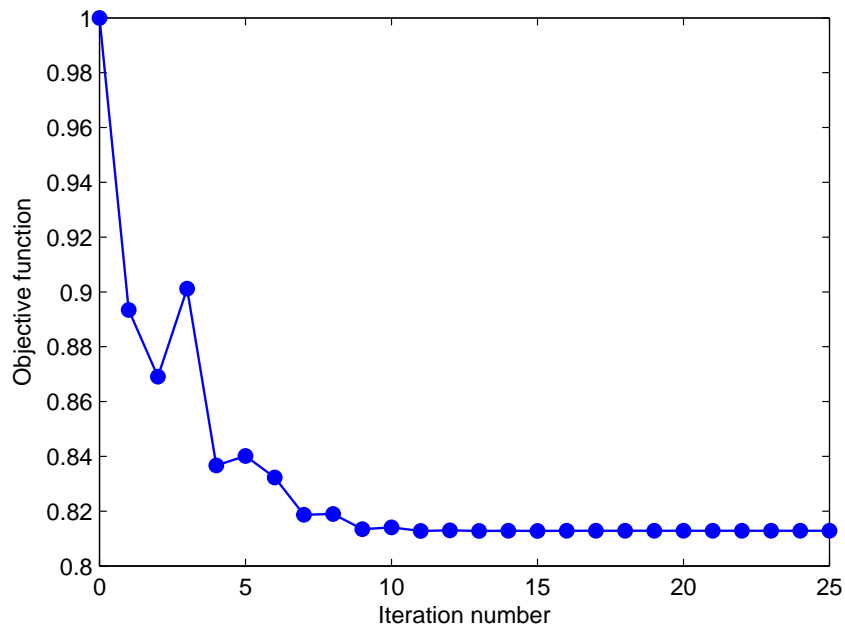


Figure 4.21: Change of the normalized objective function $\mathcal{F}(\mathbf{m})$ with iterations for the model in Figure 4.2. The inversion was performed on noise-contaminated data (see Figure 4.20).

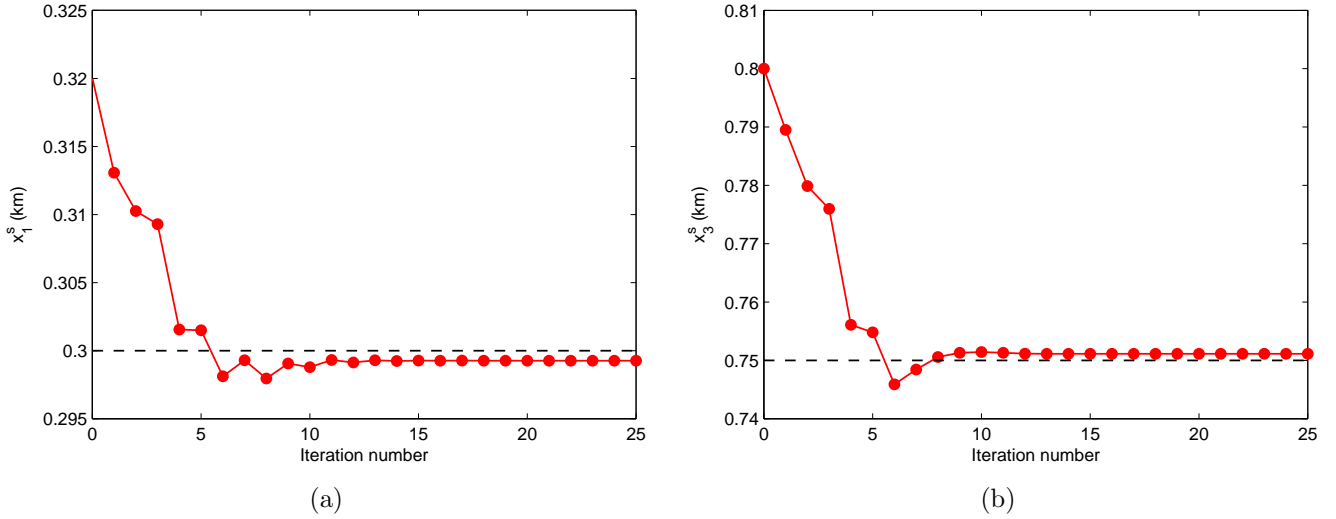


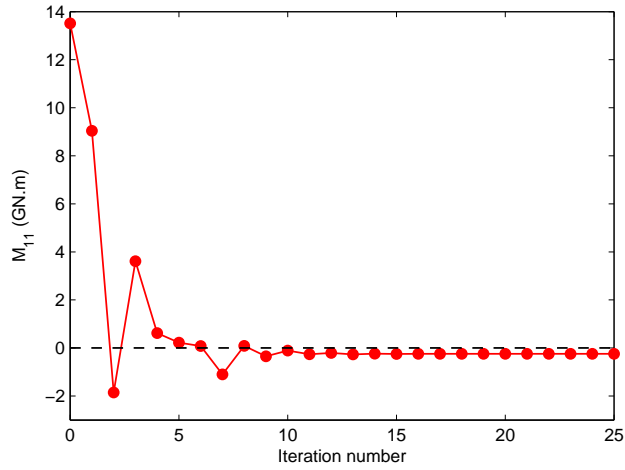
Figure 4.22: Change of the source coordinates (a) x_1^s and (b) x_3^s with iterations for the model in Figure 4.2. The inversion was performed on noise-contaminated data (see Figure 4.20).

distort mostly the tensor \mathbf{M} . However, as discussed above, the gradient for the source coordinates \mathbf{x}^s depends on \mathbf{M} , which causes small errors in x_1^s and x_3^s (Figure 4.22). Even if the variance of Gaussian noise is increased to 15% of the maximum amplitude, the inversion still produces an accurate solution.

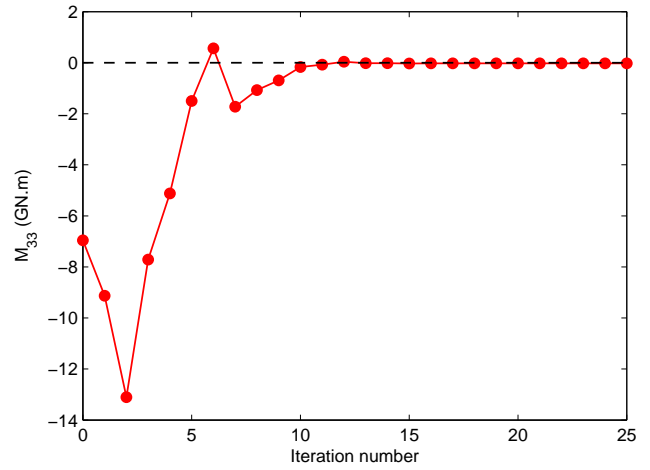
4.4 Synthetic tests with line search

The tests in the previous section were performed with a constant step length to avoid the additional cost of forward simulations required by a line-search algorithm. Because the true model in our synthetic tests is known, it is easy to select an appropriate step length to achieve fast convergence. However, implementation of this approach in practice can be problematic. It is usually more robust to compute the step length with line-search algorithms. Here, we employ the line-search equation described in Gauthier et al. (1986); Virieux and Operto (2009) and Pratt (2013):

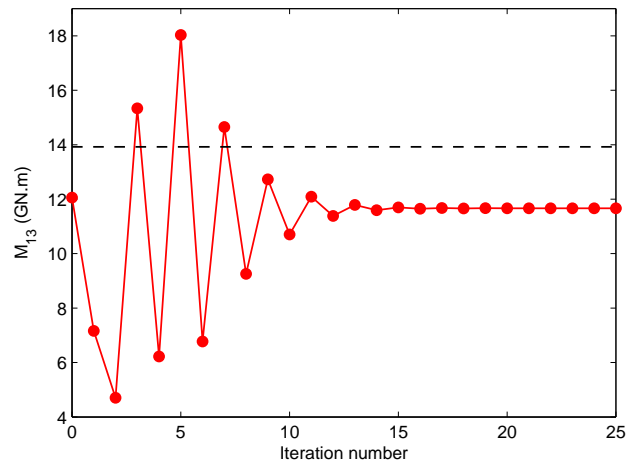
$$\alpha = \frac{(\nabla \mathcal{F})^T \mathbf{S}}{(\mathbf{JS})^T (\mathbf{JS})}, \quad (4.8)$$



(a)



(b)



(c)

Figure 4.23: Change of the moment-tensor elements (a) M_{11} , (b) M_{33} , and (c) M_{13} with iterations for the model in Figure 4.2. The inversion was performed on noise-contaminated data (see Figure 4.20).

where α is the step length, \mathbf{S} is the vector of the search direction, \mathbf{J} is the Fréchet matrix, and T stands for transpose. The product \mathbf{JS} in the denominator of equation 4.8 can be approximated by perturbing the forward displacement field $\mathbf{u}(\mathbf{m})$ using a trial step length β :

$$\mathbf{JS} = \frac{\mathbf{u}(\mathbf{m} + \beta\mathbf{S}) - \mathbf{u}(\mathbf{m})}{\beta} \quad (4.9)$$

Estimation of α is followed by minimization of the objective function using the non-linear conjugate gradient (NCG) method (Nocedal and Wright, 1999), which produces fast convergence. The NCG method used here involves the following steps (k is the iteration number):

1. Computation of the gradient direction using the adjoint-state method: $\mathbf{g}^k = \partial\mathcal{F}^k/\partial\mathbf{m}^k$.
2. Computation of the nondimensionalized model-parameter vector (equation 4.4) and scaled-gradient direction (equation 4.5).
3. Computation of β^k using the Fletcher-Reeves formula: $\beta^k = (\hat{\mathbf{g}}^k)^T \hat{\mathbf{g}}^k / [(\hat{\mathbf{g}}^{k-1})^T \hat{\mathbf{g}}^{k-1}]$.
4. Updating of the conjugate direction: $\mathbf{s}^k = \hat{\mathbf{g}}^k + \beta^k \mathbf{s}^{k-1}$ (if $k = 1$, $\mathbf{s}^{k-1} = \mathbf{s}^0 = \hat{\mathbf{g}}^k$).
5. Computation of α^k (equation 4.8).
6. Updating of the nondimensionalized model vector (equation 4.6).

The estimated conjugate direction loses accuracy with iterations and has to be reset to the gradient direction at least after every N iterations (N is the number of model parameters). The step length calculated by equation 4.8 followed by model updating using the NCG method in general provides faster convergence than a constant step length. This is due to a preconditioning operation which corrects the gradient at each iteration. For the synthetic data used here, however, the rate of convergence is similar to that achieved with a constant step length α . As mentioned above, α could be chosen in an optimal way because the model was known.

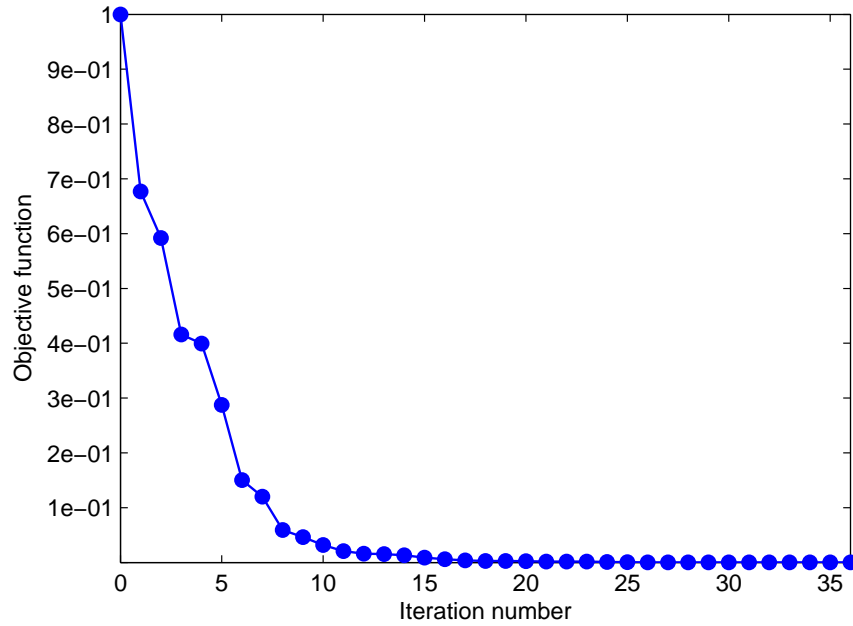


Figure 4.24: Change of the normalized objective function $\mathcal{F}(\mathbf{m})$ with iterations for the model in Figure 4.2. Parameter updating was carried out with the NCG method. The origin time t_0 is fixed at the correct value.

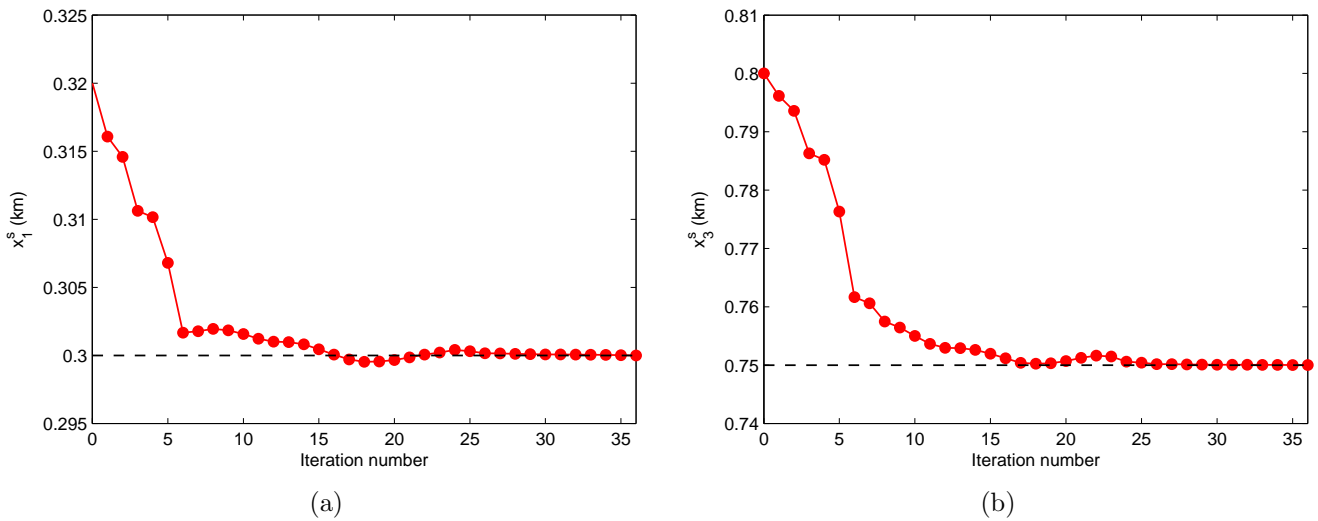
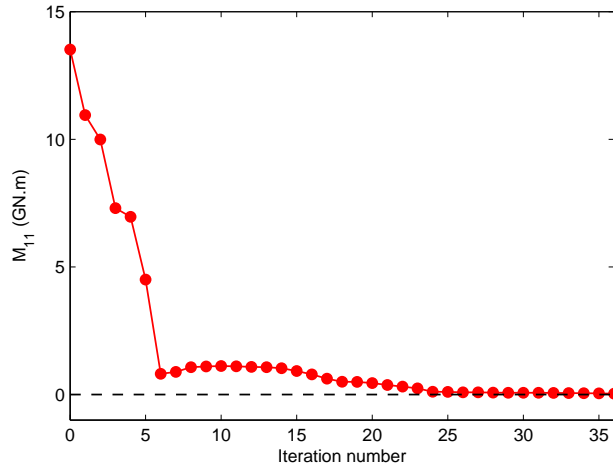
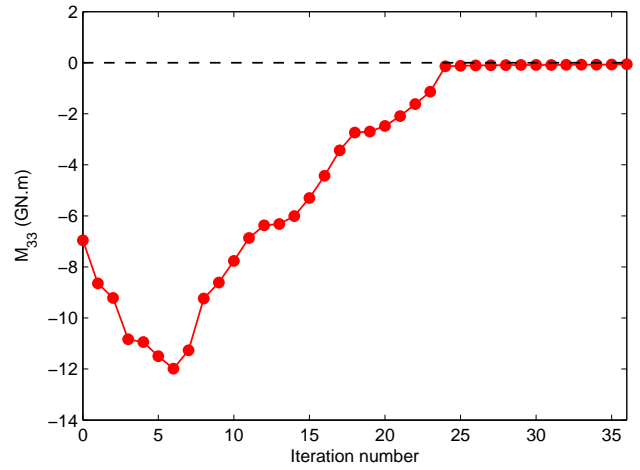


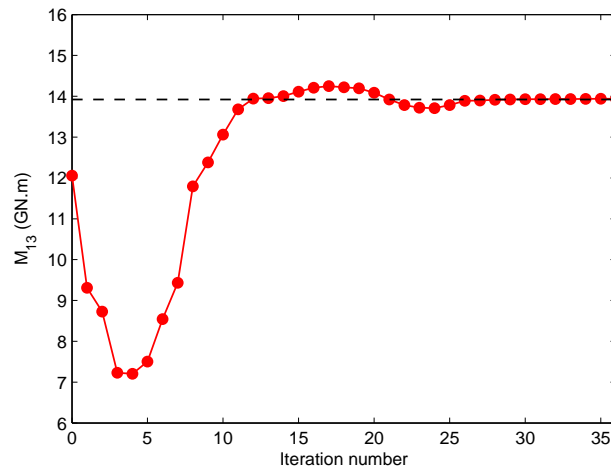
Figure 4.25: Change of the source coordinates (a) x_1^s and (b) x_3^s with iterations for the model in Figure 4.2. Parameter updating was carried out with the NCG method.



(a)



(b)



(c)

Figure 4.26: Change of the moment-tensor elements (a) M_{11} , (b) M_{33} , and (c) M_{13} with iterations for the model in Figure 4.2. Parameter updating was carried out with the NCG method.

In the following test, the parameters x_1^s , x_3^s , M_{11} , M_{13} , and M_{33} are estimated with the line-search algorithm for the model in Figure 4.2; the origin time t_0 is fixed at the actual value. The source coordinates (Figure 4.25) and moment tensor (Figure 4.26) are recovered with high accuracy, as was the case when a constant step length was used. During the first iterations, the objective function (Figure 4.24) decreases in a similar way as in the test with the constant step (Figure 4.3). However, the convergence slows down after the ninth iteration, when the estimated source position is only about 5 m away from the actual location. In that case, equation 4.8, which depends on the difference $[\mathbf{u}(\mathbf{m} + \beta\mathbf{S}) - \mathbf{u}(\mathbf{m})]/\beta$, minimizes the objective function more slowly because the location error is smaller than the grid spacing (which in this example is 6 m). Still, the model obtained after six iterations is within the limits of seismic resolution. Using a constant step length allows inversion to avoid this issue because there is no step-length calculation involved. Similar results are obtained when inverting for \mathbf{x}^s and \mathbf{M} using the model in Figure 4.10, with the origin time t_0 fixed at the correct value.

To combine the benefits of the two approaches in calculating step length, they can be applied sequentially. In the next example, \mathbf{x}^s and \mathbf{M} are estimated for the same model (Figure 4.2), with t_0 fixed at the correct value. This time, however, the NCG method with the line search is used during the first iterations and then replaced by optimization with a constant step length after the objective function has been reduced by about 80%. As shown in Figure 4.27, the objective function is minimized faster than by employing the NCG method and line search alone (Figure 4.24). The estimated source coordinates (Figure 4.28) and moment-tensor elements (Figure 4.29) are close to the actual values.

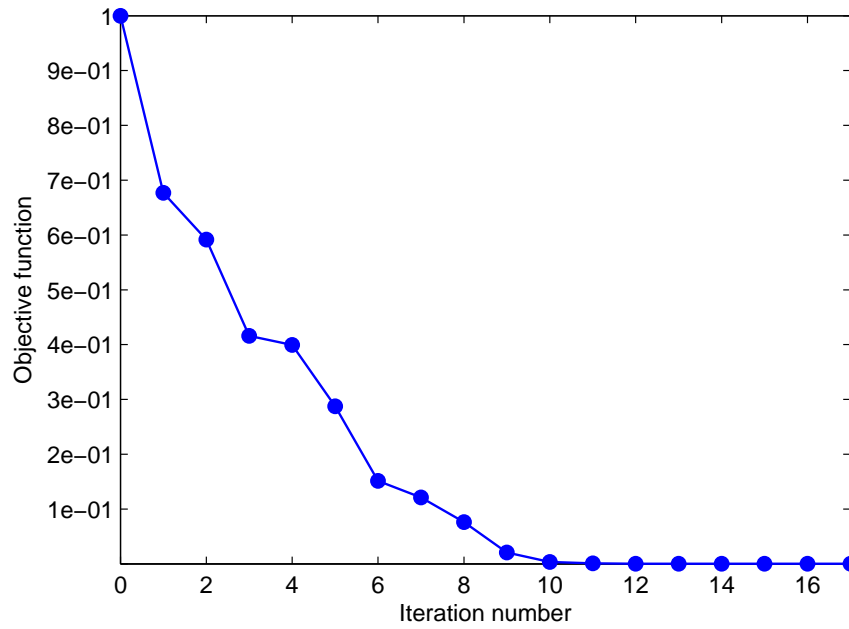


Figure 4.27: Change of the normalized objective function $\mathcal{F}(\mathbf{m})$ with iterations for the model in Figure 4.2. Parameter updating was carried out with the NCG method followed by optimization with a constant step length. The origin time t_0 is fixed at the correct value.

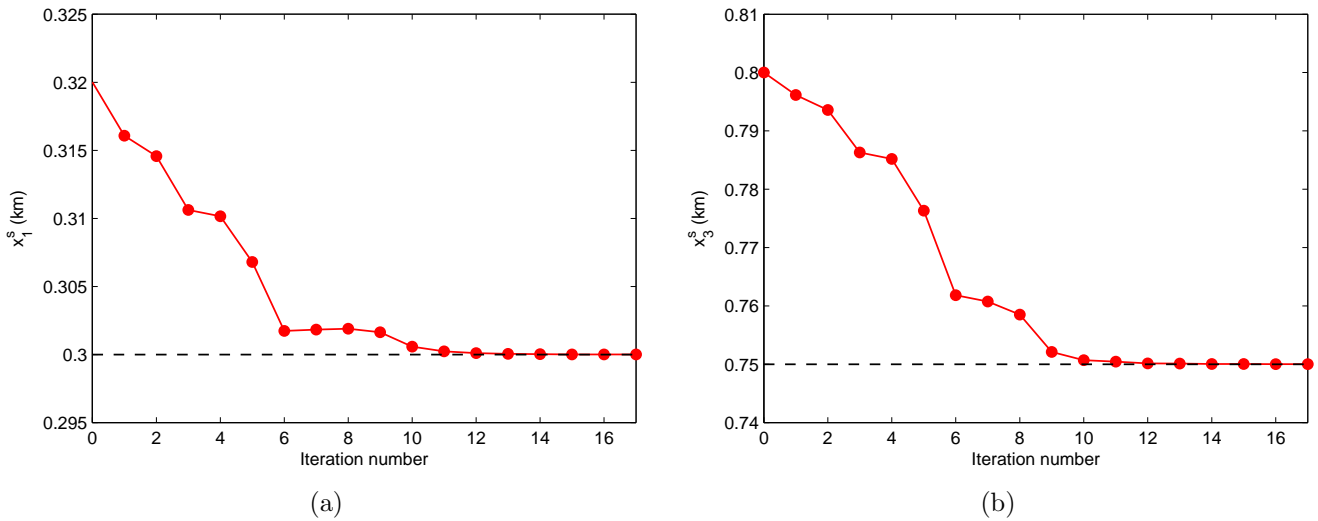
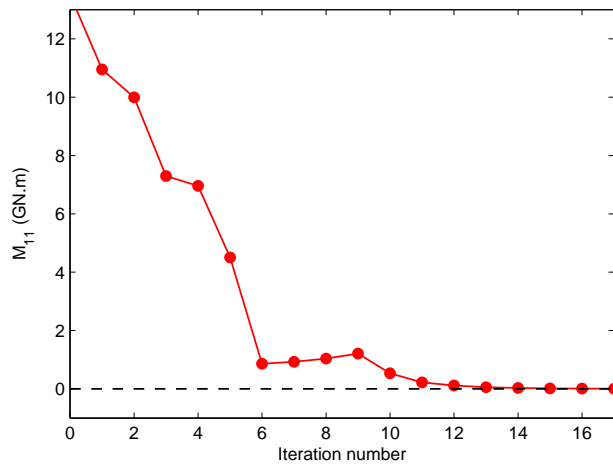
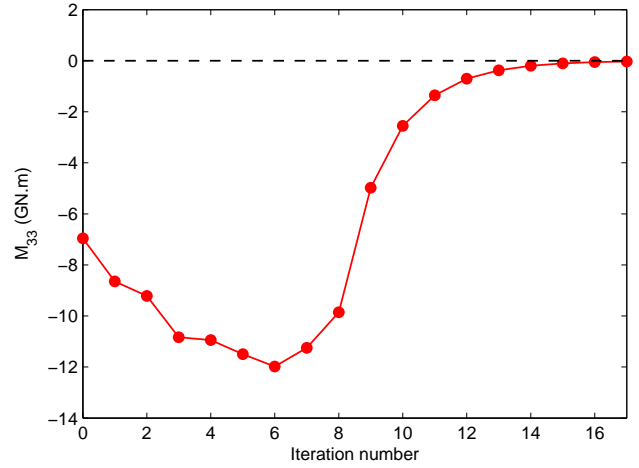


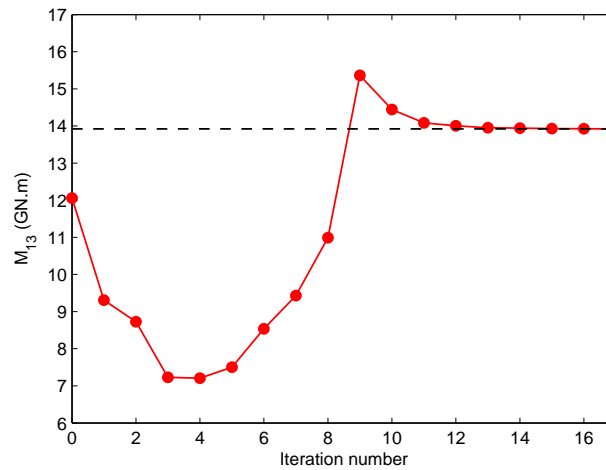
Figure 4.28: Change of the source coordinates (a) x_1^s and (b) x_3^s with iterations for the model in Figure 4.10. Parameter updating was carried out with the NCG method followed by optimization with a constant step length.



(a)



(b)



(c)

Figure 4.29: Change of the moment-tensor elements (a) M_{11} , (b) M_{33} , and (c) M_{13} with iterations for the model in Figure 4.2. Parameter updating was carried out with the NCG method followed by optimization with a constant step length.

CHAPTER 5

CONCLUSIONS AND RECOMMENDATIONS

Waveform inversion is a potentially powerful tool to solve simultaneously two of the most important problems in microseismic monitoring, event location and source-mechanism estimation. Here, the adjoint-state method was employed to find analytic expressions for the gradient of the WI objective function following the approach of Kim et al. (2011). Then adjoint simulations were implemented to calculate the WI gradient for the source location \mathbf{x}^s , origin time t_0 , and moment tensor \mathbf{M} using a known VTI velocity model.

Synthetic tests were carried out for multicomponent wavefields from one and two sources recorded by a dense array of receivers in a vertical “borehole.” The first experiment was performed for a trial source with a perturbed moment tensor correctly positioned in a homogeneous VTI medium. The adjoint wavefield focuses near the trial source location, which identifies the perturbed area. Although in this experiment the source position was correct, the derivatives for the source coordinates and origin time do not vanish because they depend on errors in the moment-tensor elements.

In the second test, a trial source with a distorted moment tensor was placed in a three-layer VTI model. The additional interfaces produce a more complicated wavefield with a number of reflected and converted waves. These additional events do not significantly influence gradient calculation but should improve the accuracy and stability of parameter estimation.

The algorithm was also tested for a source with the correct moment tensor and origin time but erroneous location in a homogeneous VTI medium. As in the previous examples, the derivatives of the objective function with respect to the correct parameters (in this case, the moment tensor and origin time) are nonzero. The dependence of the gradient on unperturbed model parameters implies that it is essential to have accurate initial guesses for

all unknowns.

The wavefield was also generated by two sources set off simultaneously, while the predicted wavefield was excited by a single source. Focusing of the adjoint wavefield helped identify the approximate location of the “missing” source. In general, if the velocity model is not strongly distorted, the adjoint wavefield can provide an accurate starting trial source position for waveform inversion.

The gradient computation provides the basis for a waveform-inversion methodology designed to estimate the source parameters of microseismic events from multicomponent data. The WI algorithm operates with the elastic wave equation for 2D heterogeneous VTI media. In addition to employing the entire trace, the WI method simultaneously inverts for parameters that are typically obtained separately by kinematic and amplitude techniques. The nondimensionalization approach was applied to handle model updating for different parameter classes.

Synthetic tests were performed for data recorded by a dense vertical array of two-component receivers in homogeneous and horizontally layered VTI media. Increasing the number of layers is actually beneficial for our algorithm because multiple reflections and conversions improve the sensitivity of WI to the source parameters. If the initial model is located within the basin of convergence, WI accurately estimates the parameters \mathbf{x}^s , t_0 , and \mathbf{M} , especially if the origin time is fixed at the correct value. Although in theory there is no trade-off between the source location and origin time, the traveltime differences responsible for resolving \mathbf{x}^s and t_0 are small near the global minimum. As a result, simultaneous inversion for the source coordinates and origin time may lead to small distortions in x_1^s and t_0 .

To evaluate the influence of errors in the velocity model, the parameters of a source in a homogeneous VTI medium were estimated using an inaccurate anisotropy coefficient ϵ (0.3 instead of 0.4). Predictably, a distortion in ϵ propagates into the horizontal source coordinate, but the error in x_1^s is not significant; the parameters x_3^s and \mathbf{M} were determined

with high accuracy.

To assess the stability of the algorithm, the input data were contaminated with Gaussian noise in the frequency band of the observed data and the variance equal to 0.07% of the maximum amplitude. Although the objective function is not reduced as much as in other tests, the only noticeably distorted parameter is M_{13} . Even if the variance of the noise reaches 15% of the maximum amplitude, the inversion results are sufficiently accurate.

Introducing a line-search algorithm for step-length calculation should improve the inversion results for field-data applications. Combining line search with the nonlinear conjugate gradient method produced a convergence rate similar to that obtained with a constant step length. In practice, however, it would be difficult to choose a constant step length in an optimal way without knowledge of the velocity model. At the last stages of inversion, it is beneficial to replace line search with constant step-length calculation because the former method is more susceptible to resolution-related limitations.

5.1 Recommendations

The WI algorithm presented in the thesis so far has been tested only on synthetic data. Application to field data is ongoing and will be reported in future publications. Seismograms recorded in the field are influenced by attenuation, 3D geometrical spreading, lateral heterogeneity, etc., which are not accounted for in the forward modeling software employed here. It is especially important to consider the difference between P- and S-wave attenuation often observed on field data. An accurate initial velocity model for WI inversion is also necessary, which can be provided by traveltimes inversion techniques.

Although the VTI velocity model was assumed known, the adjoint-state method is capable of calculating the gradient for the source and velocity parameters simultaneously. The updating procedure for the two classes of parameters takes only two modeling simulations and does not substantially increase the computational cost. Hence, to take full advantage of the adjoint-state method and WI in microseismic monitoring, they could be extended to anisotropic velocity model building. As is done in kinematic inversion, event location

can be performed simultaneously with anisotropic parameter estimation using WI. However, inverting for source locations and anisotropy parameters simultaneously may result in model-dependent trade-offs. A careful study of such trade-offs should provide a better understanding of the potential of WI in microseismic studies.

REFERENCES CITED

- Aki, K., and P. G. Richards, 1980, Quantitative seismology theory and methods, volume I: W. H. Freeman and Company.
- Dahlen, F. A., and J. Tromp, 1998, Theoretical global seismology: Princeton University Press.
- Fichtner, A., 2009, Full seismic waveform inversion for structural and source parameters: PhD thesis, Ludwig-Maximilians-Universität München.
- Fichtner, A., H.-P. Bunge, and H. Igel, 2006, The adjoint method in seismology: I. Theory: Physics of the Earth and Planetary Interiors, **157**, 86–104.
- Gauthier, O., J. Virieux, and A. Tarantola, 1986, Two-dimensional nonlinear inversion of seismic waveforms: Numerical results: Geophysics, **51**, 1387–1403.
- Grechka, V., and A. Duchkov, 2011, Narrow-angle representations of the phase and group velocities and their applications in anisotropic velocity-model building for microseismic monitoring: Geophysics, **76**, WC127–WC142.
- Grechka, V., P. Singh, and I. Das, 2011, Estimation of effective anisotropy simultaneously with locations of microseismic events: Geophysics, **76**, WC143–WC155.
- Grechka, V., and S. Yaskevich, 2013, Azimuthal anisotropy in microseismic monitoring: Part 1 Theory: SEG Technical Program Expanded Abstracts, 1987–1991.
- , 2014, Azimuthal anisotropy in microseismic monitoring: A Bakken case study: Geophysics, **79**, KS1–KS12.
- Jost, M. L., and R. B. Herrmann, 1989, A students guide to and review of moment tensors: Seismological Research Letters, **60**, 37–57.
- Kamath, N., and I. Tsvankin, 2013, Full-waveform inversion of multicomponent data for horizontally layered VTI media: Geophysics, **78**, WC113–WC121.
- Kendall, M., S. Maxwell, G. Foulger, L. Eisner, and Z. Lawrence, 2011, Microseismicity: Beyond dots in a box Introduction: Geophysics, **76**, WC1–WC3.
- Kim, Y., Q. Liu, and J. Tromp, 2011, Adjoint centroid-moment tensor inversions: Geophysical Journal International, **186**, 264–278.

- Köhn, D., 2011, Time domain 2D elastic full waveform tomography: PhD thesis, Christian-Albrechts-Universität zu Kiel.
- Lailly, P., 1983, The seismic inverse problem as a sequence of before stack migrations: Bednar, J. B., Redner, R., Robinson, E., and Weglein, A., Eds., Conference on Inverse Scattering: Theory and Application, Soc. Industr. Appl. Math., 206–220.
- Lee, H.-Y., J. M. Koo, D.-J. Min, B.-D. Kwon, and H. S. Yoo, 2010, Frequency-domain elastic full waveform inversion for VTI media: *Geophysical Journal International*, **183**, 884–904.
- Li, J., N. Toksz, C. Li, S. Morton, T. Dohmen, and K. Katahara, 2013, Locating Bakken microseismic events with simultaneous anisotropic tomography and extended double-difference method: SEG Technical Program Expanded Abstracts, 2073–2078.
- Lions, J., 1972, Nonhomogeneous boundary value problems and applications: Springer Verlag, Berlin.
- Liu, Q., and J. Tromp, 2006, Finite-frequency kernels based on adjoint methods: *Bulletin of the Seismological Society of America*, **96**, 2383–2397.
- Maxwell, S., 2010, Microseismic: Growth born from success: *The Leading Edge*, **29**, 338–343.
- Mora, P., 1987, Nonlinear two-dimensional elastic inversion of multioffset seismic data: *Geophysics*, **52**, 1211–1228.
- Morency, C., and R. J. Mellors, 2012, Full moment tensor and source location inversion based on full waveform adjoint inversion: application at the Geysers geothermal field: SEG Technical Program Expanded Abstracts, 532, 1–5.
- Nocedal, J., and S. J. Wright, 1999, Numerical optimization: Springer.
- Perrone, F., and P. Sava, 2012, Wavefield tomography based on local image correlations: CWP Project Review Report, 51–76.
- Plessix, R.-E., 2006, A review of the adjoint-state method for computing the gradient of a functional with geophysical applications: *Geophysical Journal International*, **167**, 495–503.
- Pratt, R., 1999, Seismic waveform inversion in the frequency domain, Part 1: Theory and verification in a physical scale model: *Geophysics*, **64**, 888–901.
- , 2013, *Waveform tomography an introduction to theory and practice*: Western Science.

- Talagrand, O., and P. Courtier, 1987, Variational assimilation of meteorological observations with the adjoint vorticity equation. I: Theory: Quarterly Journal of the Royal Meteorological Society, **113**, 1311–1328.
- Tarantola, A., 1984, Inversion of seismic reflection data in the acoustic approximation: Geophysics, **49**, 1259–1266.
- Thomsen, L., 1986, Weak elastic anisotropy: Geophysics, **51**, 1954–1966.
- Tromp, J., C. Tape, and Q. Liu, 2005, Seismic tomography, adjoint methods, time reversal and banana-doughnut kernels: Geophysical Journal International, **160**, 195–216.
- Tsvankin, I., 2012, Seismic signatures and analysis of reflection data in anisotropic media, third edition: Society of Exploration Geophysicists.
- Tsvankin, I., and V. Grechka, 2011, Seismology of azimuthally anisotropic media and seismic fracture characterization: Society of Exploration Geophysicists.
- Van Dok, R., B. Fuller, L. Engelbrecht, and M. Sterling, 2011, Seismic anisotropy in microseismic event location analysis: The Leading Edge, **30**, 766–770.
- Vavryčuk, V., 2005, Focal mechanisms in anisotropic media: Geophysical Journal International, **161**, 334–346.
- , 2007, On the retrieval of moment tensors from borehole data: Geophysical Prospecting, **55**, 381 – 391.
- Virieux, J., and S. Operto, 2009, An overview of full-waveform inversion in exploration geophysics: Geophysics, **74**, WCC1–WCC26.